12-1996

Demonstrating Optical Aberration Correction with a MEMS Micro-Mirror Device

Shaun R. Hick

DEMONSTRATING OPTICAL ABERRATION
CORRECTION WITH A MEMS
MICRO-MIRROR DEVICE

THESIS
Shaun Roger Hick
Captain, USAF

AFIT/GAP/ENP/96D-07

19961211 055

DTIC QUALITY INSPECTED

Approved for public release; distribution unlimited

AFIT/GAP/ENP/96D-07

DEMONSTRATING OPTICAL ABERRATION CORRECTION
WITH A MEMS MICRO-MIRROR DEVICE

THESIS

Presented to the Faculty of the School of Engineering

of the Air Force Institute of Technology

Air University

In Partial Fulfillment of the

Requirements for the Degree of

Master of Science in Applied Physics

Shaun Roger Hick, B.S.

Captain, USAF

December 1996

The views expressed in this thesis are those of the author and do not reflect the official policy or position of the Department of Defense or the U. S. Government.

AFIT/GAP/ENP/96D-07

DEMONSTRATING OPTICAL ABERRATION CORRECTION

WITH A MEMS MICRO-MIRROR DEVICE

Shaun Roger Hick, B.S.

Captain, USAF

Approved:

Michael C. Roggemann, Major, USAF Chairman, Advisory Committee	Date

Byron M. Welsh Member, Advisory Committee	Date

Victor M. Bright Member, Advisory Committee	Date

Acknowledgements

First and foremost, I wish to express my heartfelt gratitude to my wife, René, for her love and support throughout my entire time at AFIT. Without her constant reassurances, occasional prodding, and general good humor, it would have been too easy to let frustrations derail my desire to work hard. The indirect and direct motivation René provided to me allowed me to get the most out of AFIT and enjoy the experience to the fullest.

A large portion of the credit for my performance in this research belongs to my advisor, Major Mike Roggemann. His expertise in the field of adaptive optics, and his insights regarding the struggles and joys of research and writing, were indispensable to my efforts. Dr. Byron Welsh's consistent presence and willing participation throughout all the stages of my research was a pleasant surprise and a great reassurance: I felt like I must have been doing something pretty interesting for him to keep showing up voluntarily! I honestly felt like I had two, full-time advisors for this research. Of course, the cynics among us will bemoan such a scenario, but at no time did I not feel fortunate to have the attention of two overly talented and personable advisors.

This research would not have been possible without the efforts of the MEMS group in the Electrical Engineering department at AFIT, directed by Dr. Victor Bright. I thank him for the groundwork he and his students have provided to enable me to make my own contribution. Special thanks are also due to Major Bill Cowan, who personally prepared the devices I used in this research. David Blue takes the credit and my thanks for getting all the MEMS control wiring and programming completed. His patience and hard work probably kept my hair in place and saved me many sleepless nights. Finally, thanks go to Wes Bernard for taking the time to share his knowledge of operating Hartmann wave front sensors. I could not have done anything without getting the Hartmanns to work, and Wes saved me the trouble of learning it from (ugh) the manuals.

Shaun Roger Hick

iii

AFIT/GAP/ENP/96D-07

Abstract

This research conducted the first demonstrated use of a micro-electro-mechanical structure (MEMS) mirror array to correct a static optical aberration. A well developed technique in adaptive optics imaging systems uses a deformable mirror to reflect the incident wave front to the imaging stage of the system. By matching the surface of the deformable mirror to the shape of the wave front phase distortion, the reflected wave front will be less aberrated before it is imaged. Typical adaptive optics systems use piezo-electric actuated deformable mirrors. This research used an electrostatically actuated, segmented mirror array, constructed by standard MEMS fabrication techniques, to investigate its performance as a deformable mirror. The relatively cheap cost of MEMS fabrication promises new adaptive optics applications if a suitable design can be found. In the demonstration, the point spread function (PSF) of the corrected and uncorrected aberrated image were compared. A 43 percent improvement in the peak intensity of the PSF was noted in the corrected image.

Table of Contents

List of Figures

List of Tables

DEMONSTRATING OPTICAL ABERRATION CORRECTION
WITH A MEMS MICRO-MIRROR DEVICE

I. Introduction

1.1 Overview

The effects of aberrations on optical systems are well understood, and the task of compensating for aberrations is foremost in modern imaging system design. Apart from the aberrations introduced to an incident wave front from optical components, the very nature of the wave front itself may contribute to a degradation in expected performance for a given imaging system. In particular, ground-based astronomical imaging systems must deal with wave front aberrations imposed by atmospheric turbulence [1, 2]. Upon reaching the Earth's atmosphere, the light from a distant star is well represented by a plane wave, uniform in phase along planes stretching perpendicularly to the wave front's path. However, the Earth's atmosphere is decidedly non-uniform in its appearance to the wave front. The index of refraction in air is temperature dependent, and the Earth's atmosphere is characterized by a random distribution of air temperature. Thus, each portion of the originally planar wave front encounters different, randomly varying indices of refraction in its journey to the surface. By the time the wave front reaches a telescope, it is no longer planar. The primary effect is a loss of resolution: the image of the star is blurry. The consequence is that even the best telescopes cannot approach the theoretically achievable limits of their resolution.

Faced with such degrading effects, optical system designers are motivated to implement techniques for removing aberrations. The goal of adaptive optics is to compensate for aberrations by utilizing dynamic devices to remove distortions from the wave front before it reaches the final imaging stages of the system [3, 4]. A well developed technique uses a deformable mirror to reflect the incoming light to an imaging stage. By sampling the wave front and measuring the aberrations it contains, the deformable mirror can be adjusted so that the reflected wave front is more nearly planar. With the necessary processing

1

hardware, such corrections can be made to deal with temporal aberrations, such as those imposed by atmospheric turbulence.

Current implementations of such an adaptive optics system use deformable mirrors that are constructed by bonding piezo-electric actuators between a reflective surface and a rigid base plate. The surface can be continuous or segmented. Continuous mirrors tend to perform well, but are costly to make and maintain [5]. Segmented mirrors are easier to repair, but suffer performance degradation as the size of the gaps between mirrors increases [6]. In both cases, the high costs of manufacturing the mirror and the large actuator spacing limit the applications to which the technology is appropriate. Large, astronomical telescopes are well served by this technology, but a wider range of applications can be envisioned if a cheaper, smaller enabling technology can be developed.

This thesis explores the possibilities of one such enabling technology: micro-electro-mechanical structures (MEMS), individually coated with reflective material to form micro-mirror arrays. Using standard MEMS construction techniques, arrays of micro-mirrors have been constructed that can serve as a deformable mirror surface in an adaptive optics system. Each micro-mirror in the array is supported by flexure arms above a base plate. Micro-mirrors are essentially capacitors on springs: applying a voltage between the mirror and the base causes the mirror to move towards the base. The flexure arms act to provide a restoring force, and when the attractive electrical force balances the restoring mechanical force of the flexures, the mirror stops moving and maintains a static deflection for the given voltage. Each mirror is individually addressable through a separate electrode beneath each mirror.

Optical characterization of MEMS devices has been carried out through various experiments, demonstrations, and computer models, primarily at AFIT [7, 8, 9] and Texas Instruments [10, 11, 12, 13]. Past demonstrations of the optical characteristics of MEMS devices have focused on two primary areas: binary intensity filtering and beam steering. For commercial applications, binary filtering is useful for pixelized imaging systems [14, 15]. Individual micro-mirror array elements are used to reflect light towards a pixel to activate it, or away from the pixel to keep it dark. In this manner, MEMS are used as intensity modulation devices. For beam steering, MEMS arrays are used to change the phase of wave

2

front in such a way that the far field diffraction pattern has most of its power concentrated in a single lobe [16, 17, 18]. The use of MEMS in this way is as a phase modulation device.

The low cost and maturing construction techniques of MEMS devices motivates an investigation into their performance as a deformable mirror in an adaptive optics system. The goal of this research was to demonstrate the use of a MEMS device as a means to correct an optical aberration: such a use of a MEMS device has not been previously demonstrated. If micro-mirror arrays can be manufactured that perform adequately in adaptive optics systems, the potential for widespread use increases. It may become feasible to enhance existing imaging devices with small-scale, adaptive optics systems to improve performance.

Envisioned applications for the Air Force include outfitting entire space tracking networks with affordable adaptive optics systems and using MEMS deformable mirrors to beam steer laser radar devices. A line of sight optical laser communication system could use adaptive optics to correct aberrations induced by the atmosphere during transmission, with both Air Force and commercial applications. In terms of a large consumer market, amateur astronomers could use cheap adaptive optics systems on their backyard telescopes to achieve better resolution.

This is an active research area in the electro-optical community, and demonstration of aberration correction with a MEMS device is an important step in the maturing of this technology. It is expected that the results of this thesis will be used to further refine the designs of MEMS devices intended for use as deformable mirrors, hopefully resulting in future implementation of MEMS devices in a variety of adaptive optics applications.

1.2 Background

This section provides a synopsis of adaptive optics and MEMS micro-mirror developments. The adaptive optics development borrows heavily from Roggemann and Welsh [1].

1.2.1 Adaptive Optics. Using active elements, adaptive optics imaging (AOI) systems attempt to remove wave front distortions before the final imaging stage of an

3
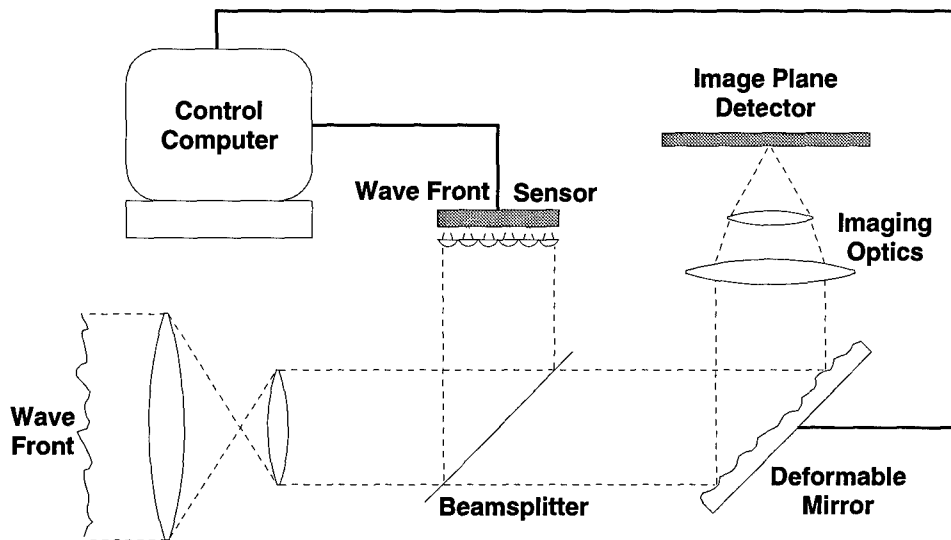
Figure 1. General optical layout for an adaptive optics system.

optical system. Aberrations represent optical path length differences between portions of the wave front. In imaging through the atmosphere, the path length differences arise from random spatial variations in the indices of refraction encountered by the wave front. Babcock was the first to state that the optical path length differences could be corrected through mechanical means, before the light is focused into an image [19]. The resulting image should be superior to an uncompensated image.

Since Babcock's introduction of the concept, AOI systems have been implemented in numerous astronomical observatories around the world. Figure 1 shows the typical layout of components used in a representative adaptive optics system. The AOI system depicted performs three basic tasks: 1) measure the aberrations on the incoming wave front, 2) adjust the deformable mirror to compensate for the distortions, and 3) form an image with the compensated wave front. The components necessary for these tasks include the wave front sensor (WFS), the deformable mirror (DM), a control computer, and the focusing components to produce the final image.

As may be inferred, the WFS performs the critical task of measuring the uncorrected wave front phase. There are two main devices used as wave front sensors in AOI systems: the shearing interferometer [20, 21] and the Hartmann wave front sensor [22, 23, 24]. Both

4

sensor types respond to the slope of the wave front phase. The Hartmann wave front sensor is abstractly depicted in Figure 1, and it was the sensor utilized in the experiments for this thesis. The details of its operation will be discussed in Section 2.4. Shearing interferometry will not be addressed further in this thesis, but it is a widely implemented technique throughout the community, including here at AFIT [25].

The DM is the component that actually performs the desired wave front correction. The DM is a reflective surface whose shape can be adjusted by electrical signals from the control computer. The DM surface is controlled so that the aberrations of the incident wave front are cancelled after reflection. Consider an incident wave front with phase $\phi\left(\vec{x}, t\right)$. Then, the field after reflection from the DM becomes [1:178],

$$
\begin{aligned}
\exp\left[i\epsilon\left(\vec{x}, t\right)\right] &= \exp\left[i\phi\left(\vec{x}, t\right)\right]\exp\left[-i\hat{\phi}\left(\vec{x}, t\right)\right], \\
&= \exp\left[i\left(\phi\left(\vec{x}, t\right) - \hat{\phi}\left(\vec{x}, t\right)\right)\right],
\end{aligned}
\tag{1}
$$

where $\vec{x}$ represents a spatial coordinate, t is time, $\phi\left(\vec{x}, t\right)$ is the piston removed wave front phase before reflection, $\hat{\phi}\left(\vec{x}, t\right)$ is the piston removed surface of the DM, and $\epsilon\left(\vec{x}, t\right)$ is the residual wave front phase after reflection. In this context, "piston" refers to the average value of the phase across the aperture of the system, so that a piston removed phase is a phase that is zero-average across the aperture. Imaging systems are insensitive to piston, and all phase quantities considered in this thesis are piston removed. In the ideal case, we desire $\phi\left(\vec{x}, t\right) = \hat{\phi}\left(\vec{x}, t\right)$ so that the residual phase is zero, and the reflected wave front is planar before it is focused by the imaging optics.

Thus, the goal of the control computer is to generate the signals necessary to match the surface of the DM to the phase of the incoming wave front. The WFS provides measurements of the slope of the phase to the computer, and the computer needs a calculation technique to map slope measurements to control signals for the DM. Wave front reconstruction refers to the techniques employed to determine the optical field phase from WFS slope measurements, and a detailed development of the technique used by this research will be given in Section 2.5. Once the phase is reconstructed, a control law is employed to determine the electrical signals to apply to the DM to match the phase.

The imaging optics focus the reflected wave front for observation. If the components work as planned, the resulting image will have better resolution than a system that imaged the incoming wave front without compensation.

Critical to the degree of success for this AOI design is the DM. Deformable mirrors may be classified as continuous or segmented. The continuous DM has a continuous mirror surface placed on top of an array of actuators. Typical construction employs piezo-electric actuators that bend the mirror surface as the actuators push and pull it in response to electrical signals to contract or expand. The primary disadvantages to such a system include the large actuator spacing required by the piezo-electric components (on the order of 1 to 2 mm between actuators), the difficulty of repair when an actuator breaks, and the complicated control laws required to form the DM to the overall desired shape. In particular, the response of each actuator is not generally independent of other actuators, and some coupling occurs. Furthermore, the deformations in the mirror surface caused by one actuator overlap regions controlled by other actuators. The result is a set of actuators that have coupled responses to input signals, and a resulting DM surface that is complicated to model and control.

Segmented deformable mirrors are formed by leaving gaps between actuators, so that the surface is composed of closely packed, individual mirror elements. This design eliminates the overlap in actuator influences that occurs with continuous DM constructions, and it is less susceptible to coupling between actuators. However, the gaps in the mirror surface lead to undesirable diffraction effects that tend to disrupt the reflected wave front from the desired planar shape. Past designs have utilized piezo-electric actuators, necessitating the same large inter-actuator spacing required in current continuous DM designs. However, piezo-electric segmented mirrors are easier to repair than their continuous DM counterpart, since individual elements can be replaced as needed [6].

1.2.2 MEMS Devices as Deformable Mirrors. Electrostatically actuated segmented mirror arrays can be fabricated on very small scales through standard micro-electro-mechanical system (MEMS) fabrication techniques [8]. Mirror to mirror spacing is on the order of 100 microns, typically smaller. The term micro-mirror array has been

applied to such devices, typically composed of tens to tens of thousands of mirrors in regularly spaced patterns. Their advantages over piezo-electric actuators include improved uniformity of response, smaller inter-actuator spacings, rapid response to changes in input signals, and significantly cheaper construction techniques.

Many different electrostatic actuator designs exist. The overall concept is to apply a voltage between a mirror segment and an underlying electrode plate so that the mirror is attracted by an individual electrode. Varying deflections can be achieved by simply changing the potential difference. This system relies on a restoring force to counteract and balance the electrostatic force. For segmented mirrors, the mirrors can be attached to posts between elements. The method of attachment is a fundamental design decision that influences the way the mirror responds to voltages. Cantilever designs attach only one side of a mirror to a post, leaving the rest unattached, so that the mirror is free to deflect towards the substrate at an angle. Torsion beams allow the mirror to twist in its mount. Flexure-beams are attached at points all around the mirror, and allow uniform deflection of the mirror towards the substrate, rather than an angled descent. In each case, the restoring force is provided by the flexure's resistance to deflection away from the equilibrium position.

As mentioned in the introduction, MEMS micro-mirror arrays can be optimized for intensity or phase modulation. To date, the method of mounting has been the primary factor in determining whether a MEMS design is suitable for a particular type of modulation [12]. Torsion beams represent intensity modulation design, reflecting portions of a wavefront towards or away from a desired direction of propagation. Flexure-beam designs are useful as phase modulators, since the mirror surface deflects uniformly relative to its mounts. Thus, adjacent mirrors can be positioned to induce a phase difference in the optical field upon reflection. Cantilever devices represent a mixture of the two types, allowing some phase and some intensity modulation.

For use as a DM in adaptive optics systems, flexure-beam designs hold the most promise. However, until recently, commercial interests have typically been in torsion and cantilever designs because of the envisioned application: pixel activation. Pixel imaging systems need a device to turn on and off various pixels in the image. To that end, micro-

mirrors can be used to reflect light towards or away from a pixel in order to turn it on or off. Micro-mirror arrays used this way become binary spatial filters. The intensity modulating nature of designs that are optimal for use in these applications have little promise for use as a DM in an AOI system.

The development of micro-mirror arrays goes back almost 20 years. In 1977, Peterson of IBM Research Laboratory published a paper describing the fabrication of a 16 element linear array of micro-mirrors by a standard silicon construction process [14]. Each mirror element appeared as a long flexure arm, free at one end to deflect towards the substrate at an angle. Peterson demonstrated the array in an optical system that simply utilized the mirrors as binary spatial light modulators to turn pixels on and off: either light was reflected towards a pixel, or it was reflected away from a pixel.

Texas Instruments (TI) was developing similar devices in the late 1970's [26:20]. In 1983, Hornbeck published a paper describing a continuous facesheet mirror, actuated by a 128 x 128 array of address electrodes [15]. Hornbeck and Pape's publication of their initial investigations into the optical properties of the continuous mirror focused on the possibility of using it as an optical Fourier transforming device [10]. Their continuous face sheet design resulted in mirror deflections that were naturally parabolic for each element. Thus, each deflected element could act as a focusing mirror for an incident beam, allowing them to explore the use of the device as an array of Fourier transformation elements. Each mirror deflection produced an individual diffraction pattern in the far-field, consisting of a dominant, single main lobe for each mirror deflection. The device, as demonstrated, would be appropriate for use in a pixel imaging system. Each pixel intensity could be controlled by the deflection of a mirror element, which affected the amount of energy in the far field main lobe for that mirror element, thus affecting the pixel intensity.

In 1987, a TI group described the construction and testing of a segmented mirror device that relied on a cantilever beam design [11]. The mirrors were linked in groups of four. By pulling down the point where the four mirrors contacted, the mirrors could be used to focus the reflected optical wave in discrete elements, in much the same way as the parabolic shaped deformation of the previously tested continuous face sheet device. Again, optical testing consisted of examining the individual lobes produced by the resulting

8

deformations, with an eye towards pixel imaging. The major drawback to the device: the active area in the device was only 35 percent of the total area.

By 1989, TI had investigated the properties of many different designs, including cantilever, torsion beam, and flexure-beam micro-mirror arrays [12]. They had achieved segmented mirror designs that had up to 80 percent active area. Recently, TI has focused on refining their flexure-beam arrays. The most recent optical demonstration involved using an interferometric microscope to illuminate a flexure-beam mirror array with coherent light at a wavelength of 546 nm [26, 13]. By deflecting certain mirrors to induce a π change in phase in the reflected beam, Lin showed certain mirrors getting dark while other stayed bright in the microscope image. Again, the intended application was binary spatial filtering.

The remaining significant work in MEMS DM device fabrication and testing has been with AFIT designed devices. AFIT started MEMS work in the early 1990's, with a variety of applications in mind. Some of the early research was performed using and characterizing TI devices [7], but AFIT quickly moved to designing and contracting for fabrication of our own devices. Comtois's Ph.D. dissertation explored a multitude of design issues for MEMS devices, including optical applications for micro-mirror arrays [8]. In the same time frame, Michalicek presented and tested a device characterization model to explore mirror deflection vs. voltage applied for flexure-beam designs [9]. Using Comtois's design methodology and Michalicek's device model, Christensen demonstrated optical beam shaping of laser diode array outputs using a linear array of micro-mirror devices to affect the diffraction orders in the far field [16].

An AFIT and University of Dayton (UD) team utilized AFIT devices to demonstrate beam shaping and steering of a reflected laser wave front [17]. They benchmarked their experimental results against modeling published earlier by UD and Wright Laboratories at Wright-Patterson AFB [18, 27]. During the same time frame as this thesis research was performed, Roberts developed a highly detailed model of the far field patterns produced by MEMS devices used as deformable mirrors [28]. The various demonstrations and models have shown that it is feasible to modify the central lobe of the far field diffraction pattern

in beneficial ways. These efforts lay the foundation for the demonstration performed in this research.

1.3   Research Objectives and Approach

The goal of this research was to demonstrate the use of a MEMS micro-mirror array to correct an optical aberration. The scope of the research was limited to attempting to correct a static aberration with an available MEMS device. It was not expected that complete correction of an aberration could be achieved with the devices available: the degree of success was to be determined by the research.

The actual MEMS device used was a flexure-beam design by Comtois. Comtois wanted to make an array with closely packed mirrors, to maximize active surface area. To that end, he chose a hexagonal design, both for the mirror surfaces and their array geometry. A scanning electron microscope (SEM) image in Figure 2 shows the entire array of mirrors used in this demonstration. Figure 3 is an enlargement showing a single mirror and the detail of its flexure arm geometry. The active area of the design is 48 percent: not very large compared to some recent TI designs. Although the mirrors may appear planar, subsequent measurements with an interferometric microscope indicated each mirror in the array was parabolic, tending to focus reflected light.

The fundamental experiment methodology was to use a plane wave and plane mirror for reference reflection measurements, then use a long focal length lens to introduce a slight, spherical aberration to the plane wave. The resulting aberration was measured with a wave front sensor, and appropriate voltages were calculated to match the MEMS shape to the aberration. By imaging the MEMS reflections, the resulting distribution of image intensity was compared for corrected and uncorrected cases. The ideal image should be of a single point, but the diffraction limited image will be something quite different, especially for a MEMS reflection. An improved image should be detectable by examining the intensity distribution in the central diffraction order. Wave fronts with large aberrations produce central diffraction intensity distributions that are lower in peak intensity and are more spread out than the image produced by a less aberrated wave.
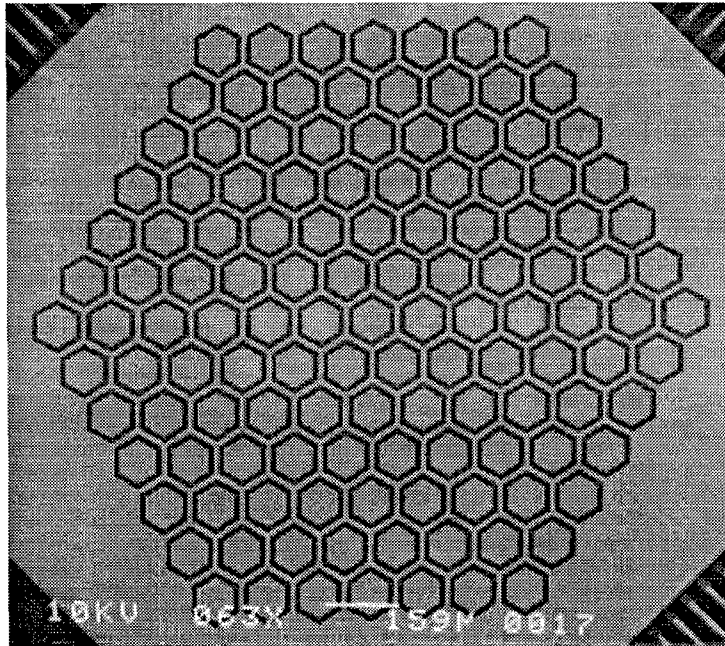
Figure 2.   A SEM image of the entire MEMS micro-mirror array used in this research. There are 127 mirror elements.
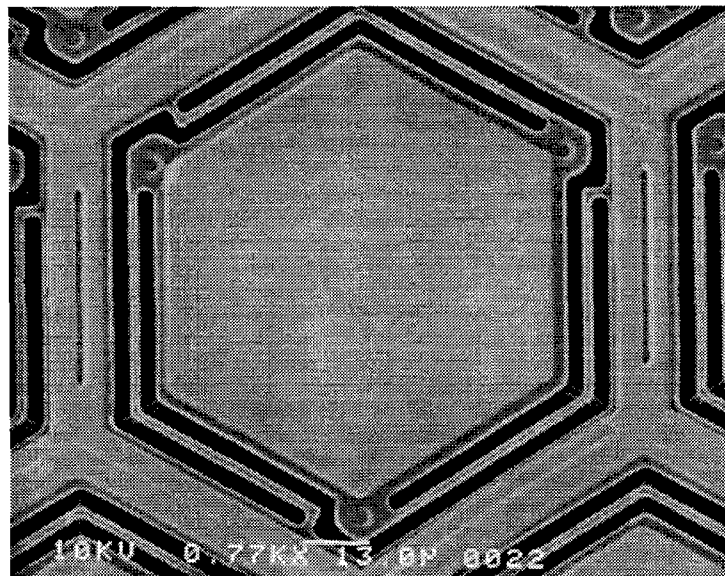
Figure 3.   A higher magnification SEM image showing a single mirror and the details of its flexure arms.
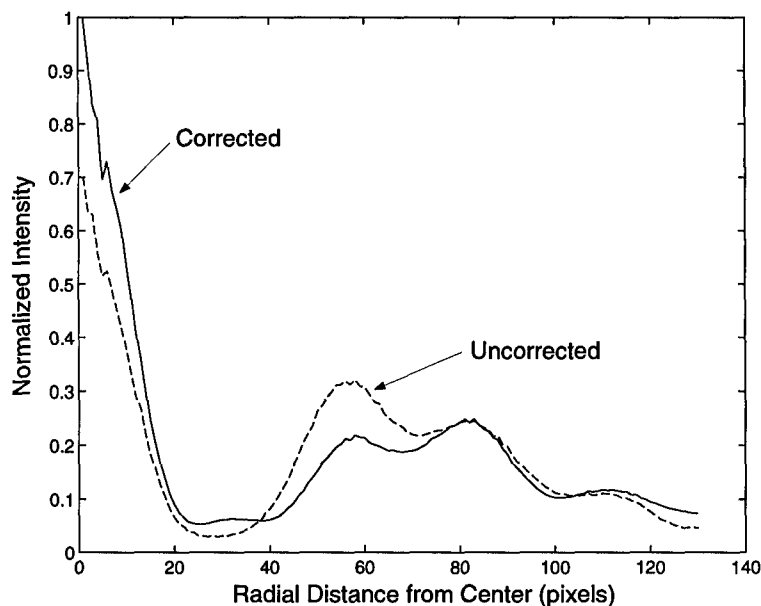
Figure 4. Comparison of the radial average PSF intensity for the corrected and uncorrected aberration MEMS reflections, where the uncorrected case is for the MEMS in an undeflected position.

Thus, success will be indicated by the comparison of the central diffraction orders of the corrected and uncorrected wave fronts.

1.4 Summary of Key Results

The demonstration was able to show the expected improvements in the point-spread function (PSF) of a spherically aberrated plane wave by using the MEMS mirror array as a deformable mirror to correct the incident aberration. This was the first known demonstration of its kind. Figure 4 shows a comparison of the radial average PSF intensity distributions for a corrected and uncorrected MEMS reflection. The curves have been normalized to the peak value of the corrected wave front. The changes we wish to observe are qualitative improvements in the PSF. The most dramatic features of note are the nearly 43 percent rise in peak intensity of the central lobe, and a reduction in the relative intensity of the off-center lobes: in the uncorrected case, the lobes are much higher in relative intensity to the central peak. We see that the corrected case has lowered the off-center peak values

12

relative to the central peak. These changes are consistent with a reduction in the degree of aberration.

Additionally, the corrected pattern has enhanced the first Airy-like ring of the PSF. Note that the solid line (corrected reflection) in Figure 4 has a slight hump in it after the initial drop to zero from the central peak. The feature is noticeably absent from the dashed line (uncorrected reflection). This feature is present in the unaberrated PSF, and its reappearance in the corrected reflection is encouraging.

However, the corrected reflection peak intensity is only 0.14 times the peak intensity measured from an unaberrated plane wave reflection off the MEMS. Based on modeling performed by Roberts, we did not expect to achieve total correction of the aberration with the devices available [28]. In fact, our results are in excellent agreement with his modeling results, which predicted a corrected peak value of about 0.15 the unaberrated peak value. The primary limitation to achieving better results was the low active surface area of the device used in this research: only 48 percent active area. However, we have a next generation design that will compensate for some of the shortcomings of the inherent, small active area in MEMS devices (see the *Conclusions and Recommendations* chapter).

1.5   Thesis Organization

This introduction has developed the material necessary to provide a background from which the rest of the thesis will be presented. The contents of the remaining chapters are outlined below. In brief, relevant theoretical developments are dealt with in the next chapter, followed by the experiment setup and methodology. The experiment results are presented next, followed by the conclusions and recommendations of the research.

- **Theoretical Background**

  This section develops the relevant theory necessary to conduct elements of the experiment and analyze the data. It starts by stating some concepts and results of Fourier optics that will be utilized throughout the thesis and data analysis. Next, the theoretical use of a Hartmann wave front sensor is addressed, including a development of the limitations in using such a sensor to measure MEMS reflections.

Subsequently, the use of wave front slope measurements to reconstruct the original wave front phase is covered. Finally, the theory of MEMS mirror deflections is addressed, focusing on the control equation used to calculate the required voltages to achieve desired deflections.

- **Experiment Methodology**

  The next chapter presents the experimental arrangement, components, and procedures used to collect the data. The final setup is presented and explained, followed by an account of the various procedures and algorithms used to collect and analyze the data.

- **Analysis and Results**

  The results of the aberration correction demonstration are presented in this chapter. The results are presented in a variety of graphical forms, including recorded images of intensity distributions, and plots of radial average intensities for reference, corrected, and uncorrected wave fronts.

- **Conclusions and Recommendations**

  A summary of the results is presented, along with recommendations for future developments in using MEMS micro-mirror arrays for aberration corrections.

II. Theoretical Background

2.1 Overview

This chapter starts by setting out some results from Fourier analysis and linear systems theory that will be important for later analysis. Although it is hoped that the reader is already familiar with the topic of Fourier optics, the results presented in the next section emphasize the concepts crucial to this thesis, particularly that of the point spread function and its response to system aberrations. There are many good texts which develop the results presented in the first two sections[29, 30], and they should be consulted for more detailed derivations.

Next, the theory of the Hartmann wave front sensor is developed, including an analysis of its limitations with respect to measuring the discontinuous fields associated with a MEMS reflection. The Hartmann sensor measures the wave front slopes, and the wave front phase must be reconstructed from these slope measurements; this reconstruction process is the topic of the next section. Finally, the necessary control equation is presented that establishes how the MEMS mirror elements respond to an applied voltage.

2.2 Fourier Transforms and Linear Systems

The Fourier transform of a function of two independent variables is defined by [29:306],

$$\mathcal{F}\{g\} \equiv \int_{-\infty}^{\infty} \int_{-\infty}^{\infty} g(x,y) \exp\left[-i2\pi(f_x x + f_y y)\right] dx\, dy, \tag{2}$$

where x and y are the independent variables of g. The resulting Fourier transform is now a function of f_x and f_y, represented by $G(f_x, f_y)$. The original function can be recovered by the inverse Fourier transform [29:306],

$$\mathcal{F}^{-1}\{G\} \equiv \int_{-\infty}^{\infty} \int_{-\infty}^{\infty} G(f_x, f_y) \exp\left[i2\pi(f_x x + f_y y)\right] df_x\, df_y, \tag{3}$$

so that $g(x,y) = \mathcal{F}^{-1}\{G\}$. The general interpretation of the Fourier transform is that it represents the frequency spectrum of a function, the frequency units being the inverse of the units of the original independent variables. For the case where the independent

15

variable is time (in seconds), the frequency unit is the expected Hertz (inverse seconds). For spatial independent variables measured in meters, the independent variable of the Fourier transform is a spatial frequency, measured in inverse meters.

The basic properties of Fourier transforms may be found in any good reference on the topic, and are usually listed wholesale in extensive tables [29:313–317]. It is assumed that the reader is familiar with the most general properties (e.g. shift theorem, linearity theorem, scaling theorem, etc.), and they will not be restated here, but they will simply be cited and used when convenient. The most important relation for further theoretical developments in this thesis is the relation between the Fourier transform and the convolution operation. Recall that the convolution of two-dimensional functions is an integral equation defined as [29:291],

$$g_1 * g_2 \equiv \int_{-\infty}^{\infty} \int_{-\infty}^{\infty} g_1(x,y) g_2(x - \alpha, y - \beta) d\alpha \, d\beta, \tag{4}$$

where x and y are the independent variables, and α and β are dummy variables of integration. If $g(x,y)$ represents the convolution of two functions $f(x,y)$ and $h(x,y)$,

$$g \equiv f * h, \tag{5}$$

then let G, H, and F represent their respective Fourier transforms. It can be shown [29:314],

$$G(f_x, f_y) = F(f_x, f_y) H(f_x, f_y), \tag{6}$$

so that the Fourier transform of g is simply the product of the Fourier transforms of each individual function in the convolution.

Convolution turns out to be an important operation that relates the output to the input of a linear, shift-invariant system [30:19–22]. A system is *linear* if its output is linearly proportional to its input, and it is *shift-invariant* if a shift in the input coordinates causes only a shift in the location of the output, not a change in the functional form. In particular, if $g_2(x,y)$ is the output of a system at coordinates (x,y), and $g_1(u,v)$ is the

16

input to the system at coordinates (u, v), the two are related by [30:21],

$$g_2 = g_1 * h, \qquad (7)$$

where h is called the *impulse response* of the system, and is a function of (x, y, u, v). The impulse response is the output of the system in response to a δ function input. If $\mathcal{S}$ is the mathematical operator that represents the response of a system to any input, then [30:20],

$$h(x, y, u, v) = \mathcal{S}\left\{\delta(x - u, y - v)\right\}. \qquad (8)$$

The convolution relationship between the input and the output implies that the techniques of Fourier transforms may be used to relate the input and output in the frequency domain. Applying Equation 6 to Equation 7,

$$G_2(f_x, f_y) = G_1(f_x, f_y)H(f_x, f_y), \qquad (9)$$

where the function H is called the *transfer function* of the system and is simply the Fourier transform of the impulse response, h. By performing calculations in the frequency domain, the relationship between input and output of a linear, shift-invariant system is obtained by simple multiplications with the transfer function. This has a computational and conceptual advantage for certain calculations involving these types of systems.

As shown by Goodman [30], optical imaging systems are linear and shift-invariant. Thus, the full power of Fourier transform techniques may be brought to bear on solving problems where the image field (i.e. output of the system) is desired as a function of the object field (i.e. the input to the system). The following section develops some of the applicable results using the relationships outlined above.

2.3   Fourier Optics

This section starts by developing the Fourier transform approach for calculating the optical field at an observation point a distance away from the source field. Then, the Fourier transforming property of lenses is explored. Next, a development of the point

17
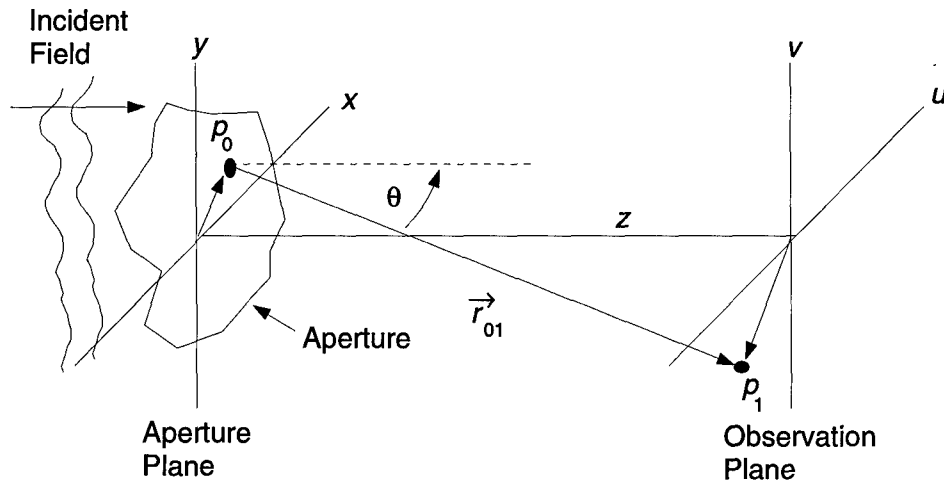
Figure 5. Coordinate system geometry for development of diffraction theory.

spread function for a single lens imaging a distant point source is presented. Finally, the effect of aberrations on the point spread function is discussed.

2.3.1 Diffraction.   Consider the geometry shown in Figure 5. On the left, the field is incident upon an aperture in the xy plane. We wish to find the resulting field in the observation plane, a distance z away. The results presented employ scalar diffraction theory, where the optical field representations are treated as scalar quantities and their vector nature is ignored. Scalar diffraction theory is accurate if the aperture is large compared to the optical wavelength, and if the observation plane is many wavelengths away from the diffracting plane [30].

Returning to Figure 5, the vector $\vec{r}_{01}$ links the source point $p_0 = (x, y)$ to the observation point $p_1 = (u, v)$. The Rayleigh-Summerfield diffraction formula describes the resulting field in the uv plane [30:50],

$$g_i (u, v) = \frac{1}{i\lambda} \int \int g_o (x, y) \frac{\exp (ikr_{01})}{|\vec{r}_{01}|} \cos \theta \, dx \, dy, \tag{10}$$

where $g_i (u, v)$ is the field in the observation plane and $g_o (x, y)$ is the field in the aperture plane, both in complex phasor representation, λ is the optical wavelength, k is the wave number $(2\pi/\lambda)$, and the integration is over the entire xy plane. The $\cos \theta$ term is the

18

obliquity factor. Equation 10 is the solution to the Helmholtz wave equation for the problem geometry. The wave equation is solved by use of Green's theorem and a correct choice of a Green's function [30:46–50].

From the geometry of Figure 5, it is seen that the following relationships hold:

$$\cos\theta = \frac{z}{r_{01}} \tag{11}$$

$$r_{01} = \sqrt{z^2 + (u-x)^2 + (v-y)^2}. \tag{12}$$

We see that Equation 10 is now explicitly a function of (x, y, z, u, v). An approximation can be made to further simplify Equation 10 by using a binomial expansion on r_{01} and keeping only the first few terms, where appropriate (see Goodman for the details) [30:66–67]. In the Fresnel approximation, we assume that $z \gg (u-x)$ and $z \gg (v-y)$. Substituting Equations 11 and 12 into Equation 10 and using the Fresnel approximation, the Fresnel diffraction formula becomes [30:67],

$$g_i(u,v) = \frac{e^{ikz}}{i\lambda z} e^{i\frac{k}{2z}(u^2+v^2)} \int \int \left\{ g_o(x,y) P(x,y) e^{-i\frac{k}{2z}(x^2+y^2)} \right\} e^{-i\frac{2\pi}{\lambda z}(ux+vy)} dx\, dy, \tag{13}$$

where $P(x,y)$ is the pupil function representing the finite extent of the aperture. $P(x,y)$ has a value of unity inside the aperture, and zero outside, so that the limits of integration in Equation 13 may be taken as $(-\infty, \infty)$. A moment's inspection will show that (aside from some multiplicative constants) the expression in Equation 13 is a Fourier transform of the product of the terms in curly brackets: the incident field, the pupil function, and a quadratic phase exponential.

The Fresnel approximation holds for the assumptions that allow the use of scalar diffraction theory, in particular $z \gg \lambda$, which is not very restrictive since λ is on the order of a few hundred nanometers for optical wavelengths. Thus, Equation 13 is used for so-called *near field* calculations. When observations occur at a relatively large distance from the aperture plane, a further simplification can be made in Equation 13. Consider the situation where

$$z \gg \frac{k(u^2+v^2)_{\text{max}}}{2}, \tag{14}$$

19

is satisfied. Then, the quadratic phase exponential inside the integral of Equation 13 is approximately unity over the entire aperture. The field in the observation plane can be written [30:74],

$$g_i(u,v) = \left. \frac{e^{ikz}e^{i\frac{k}{2z}(u^2+v^2)}}{i\lambda z} \mathcal{F}\{g_o(x,y)P(x,y)\}\right|_{f_x = \frac{u}{\lambda z}, f_y = \frac{v}{\lambda z}}, \qquad (15)$$

which explicitly shows the Fourier transform relationship between $g_i(u,v)$, $g_o(x,y)$, and $P(x,y)$. The field predicted by Equation 15 is referred to as the *far field* or *Fraunhofer diffraction pattern*.

What has been shown is remarkable: the far field diffraction pattern is proportional to the Fourier transform of the aperture field distribution! The next step is to consider the effects of lenses on a propagating optical field.

2.3.2 Lenses. Goodman provides a nice derivation of the phase transforming properties of lenses [30:96–100]. The result is that if $g_o(x,y)$ is the field incident on a lens in the xy plane, the field $g_l(x,y)$ just past the lens is given by [30:99],

$$g_l(x,y) = g_o(x,y) \exp\left[-i\frac{k}{2f}(x^2+y^2)\right], \qquad (16)$$

where f is the focal length of the lens. We may interpret the exponential term as a quadratic approximation to a spherical wave. We then see that the effect of a lens is to impart a spherical radius of curvature to the incident field. For positive f, the lens causes the incident field to be more convergent in the positive z direction, while negative f lenses cause the field to be more divergent. Equation 16 ignores the finite extent of the lens.

To establish the effect of the finite extent of the lens, consider a single, positive focal length lens. Let $g_o(x,y)$ be the field incident on the lens, and let $P(x,y)$ be the lens pupil function. To find the field distribution $g_f(u,v)$ in the back focal plane of the lens, use Equation 16 to find the field just past the lens, and then apply the Fresnel diffraction

20

formula from Equation 13 to obtain [30:103],

$$g_f(u,v) = \frac{e^{ikf}\exp\left[i\frac{k}{2f}(u^2+v^2)\right]}{i\lambda f} \times$$
$$\int\int g_o(x,y)P(x,y)\exp\left[-i\frac{2\pi}{\lambda f}(xu+yv)\right]dx\,dy. \tag{17}$$

This is immediately recognized as a Fourier transform relationship, such that,

$$g_f(u,v) = \frac{e^{ikf}\exp\left[i\frac{k}{2f}(u^2+v^2)\right]}{i\lambda f}\mathcal{F}\{g_o(x,y)P(x,y)\}\Bigg|_{f_x=\frac{u}{\lambda f},f_y=\frac{v}{\lambda f}}. \tag{18}$$

If the extent of the incident field is less than the dimensions of the lens, $P(x,y)$ is irrelevant to the calculation and can be set to unity. Then, the lens acts as a Fourier transforming device for the incident optical field. Comparing to Equation 15, the field distribution in the focal plane of the lens is just the Fraunhofer diffraction pattern of the apertured field incident on the lens, even though the observation plane is only a distance f away from the plane of the lens. Thus, a lens may also be viewed as a means of observing the far field diffraction pattern of a field within a reasonable observation distance. The two views are equivalent.

2.3.3 Point Spread Function.   The geometrical optics view of a lens is as an imaging element. Real imaging systems may be composed of many lenses, used in combination to correct aberrations in the lenses themselves, or to achieve certain magnifications at a desired imaging location. An imaging system is *diffraction limited* if a diverging spherical wave, emanating from a point-source object, is converted by the system into a converging spherical wave, and if all points in a common object plane are related to points in a common image plane by the same magnification factor [30:128]. Our model of a single lens, as contained in Equation 16, fits this definition. Without a loss of generality, a single, positive focal length lens may be used as a model of a diffraction limited imaging system to explore the effects of aberrations on the image produced.

The relationship between the object and image plane locations for a single lens is contained in the equation [30:110],

$$\frac{1}{f} = \frac{1}{z_o} + \frac{1}{z_i}, \tag{19}$$

where f is the focal length of the lens, z_o is the distance from the object plane to the lens, and z_i is the distance from the lens to the image plane. For astronomical imaging systems, the object location may be taken as infinity, placing the image plane at the back focal plane of the lens. Thus, for astronomical imaging conditions, Equation 18 describes the diffraction limited image field produced by a single lens.

The wave-optics view of the scenario is that the wave front reaching the lens from a distant source is closely approximated by a plane wave. Neglecting the finite extent of the lens, we may use Equation 16 to calculate the field just past the lens. We see that an incident plane wave of arbitrary amplitude $g_o = A$ is transformed into a converging spherical wave $g_l = A \exp\left[-i\frac{k}{2f}(x^2 + y^2)\right]$ of radius f: the wave will converge to a point at the back focal plane of the lens. Using Equation 18 to now take into account the finite nature of the lens, we set $g_o = A$, then [30:103],

$$g_f(u,v) = A \left.\frac{e^{ikf} \exp\left[i\frac{k}{2f}(u^2 + v^2)\right]}{i\lambda f} \mathcal{F}\{P(x,y)\}\right|_{f_x = \frac{u}{\lambda f}, f_y = \frac{v}{\lambda f}}, \tag{20}$$

and we see that the diffraction limited field produced in the focal plane, $g_f(u,v)$, will be proportional to the Fourier transform of the lens pupil function. The resulting intensity distribution, I_f, is given by the modulus squared of Equation 20,

$$I_f = |g_f(u,v)|^2 = \left.\left|\frac{A}{\lambda f}\mathcal{F}\{P(x,y)\}\right|^2\right|_{f_x = \frac{u}{\lambda f}, f_y = \frac{v}{\lambda f}}. \tag{21}$$

This is the intensity pattern predicted for imaging a distant point source.

Goodman has shown that imaging systems are linear-shift invariant. Thus, the image produced by a lens can also be predicted by a convolution between an input field and an

impulse response function, such that [30:113],

$$g_i(u,v) = g_g(u,v) * h_l(u,v) \tag{22}$$

where $g_g(u,v)$ is the geometrical optics prediction of the field and $h_l(u,v)$ is the desired impulse response. $g_g(u,v)$ is defined in terms of the incident field by a simple scaling relationship [30:113],

$$g_g(u,v) = \frac{1}{|M|} g_o\left(\frac{u}{M}, \frac{v}{M}\right), \tag{23}$$

where M is the magnification predicted by geometrical optics ($M = -z_i/z_o$).

Goodman derives the impulse response for an imaging system and shows it to be [30:130],

$$
\begin{aligned}
h_l(u,v) &= \frac{1}{\lambda z_2} \int \int P(x,y) \exp\left[-i\frac{2\pi}{\lambda z_2}(ux+vy)\right] dx\, dy, \\
&= \frac{1}{\lambda z_2} \mathcal{F}\{P(x,y)\}\Big|_{f_x = \frac{u}{\lambda z_2}, f_y = \frac{v}{\lambda z_2}},
\end{aligned} \tag{24}
$$

where z_2 is the distance from the lens to the uv image plane, and the integral has been explicitly identified as the Fourier transform of the lens pupil function. By definition, the impulse response of Equation 24 is the image field predicted for a delta function input. In optics, a delta function input is synonymous with a point source object. If a point source is located infinitely far away, so that the image location is $z_2 = f$, then the intensity distribution, $I(u,v)$, predicted by Equation 24 will be,

$$I(u,v) = |h_l(u,v)|^2 = \left|\frac{1}{\lambda f}\mathcal{F}\{P(x,y)\}\right|^2_{f_x = \frac{u}{\lambda f}, f_y = \frac{v}{\lambda f}}. \tag{25}$$

Comparing this result to the intensity predicted by Equation 21, we see the expressions are identical for unit amplitude inputs ($A = 1$), justifying our interpretation of the impulse response for an imaging system as the intensity distribution produced from imaging a point source object.

In optics, the intensity predicted by the impulse response is given the special name of *point spread function*, abbreviated by PSF [30:20]. As implied by the name, the PSF is the intensity distribution produced by an imaging system in response to a point source of light. By deriving the form of the PSF through the impulse response, we know how the system will respond to point sources of light. Referencing Equation 22, the field produced for an extended object is seen to be the convolution of the geometrical optics prediction of the field with the imaging system impulse response.

For this research, all the images produced will be for plane wave inputs, the functional equivalent of imaging distant point-source objects. Explicitly, the PSF predicts the images produced by,

$$\text{PSF} = \left| h_l\left(u, v\right) \right|^2 = \left| g_f\left(u, v\right) \right|^2, \tag{26}$$

and we can now explore the changes that will result in the PSF due to aberrations.

2.3.4 Aberrations.   Now consider adding an element to an optical system that causes aberrations in incident wave fronts before they reach the imaging lens. For ground-based astronomical imaging systems, the unaberrated, incident wave front will be planar, and the aberrating element will be the atmosphere. Let the phase aberration at the lens plane be represented by $a(x, y)$ so that the field incident on the lens is given by,

$$g_o\left(x, y\right) = e^{ia(x,y)}. \tag{27}$$

Using Equation 18 to predict the subsequent image field in the focal plane of the lens,

$$g_f\left(u, v\right) = \frac{e^{ikf} \exp\left[i\frac{k}{2f}(u^2 + v^2)\right]}{i\lambda f} \mathcal{F}\left\{e^{ia(x,y)} P\left(x, y\right)\right\}\Bigg|_{f_x = \frac{u}{\lambda f}, f_y = \frac{v}{\lambda f}}, \tag{28}$$

we see that the field will be proportional to the Fourier transform of the product of the aberrated field and the pupil function for the lens. From a physical standpoint, this is equivalent to associating the aberration with the pupil function of the lens and assuming an unaberrated plane wave actually reached the lens. Thus, we can define a *generalized pupil*

function, $W(x, y)$, that acts to put the aberration $a(x, y)$ on any incident, unaberrated wave front [30:145].

Using the generalized pupil function in Equation 26 to define the PSF for an aberrated system, we see,

$$\text{PSF} = \left| \left(\frac{1}{\lambda z_2} \right) \mathcal{F} \{ W(x, y) \} \right|^2_{f_x = \frac{u}{\lambda z_2}, f_y = \frac{v}{\lambda z_2}}, \tag{29}$$

where the Fourier transform nature of the PSF has been made explicit. We now have a PSF that predicts the image of an aberrated point source. Of course, for a distant point source, we set $z_2 = f$ for the aberrated PSF. Comparing the result to the focal plane intensity that would be predicted by taking the modulus squared of Equation 28, we see that they are the same. Thus, in our experiment, we can simply examine the focal plane intensity distribution to determine the PSF for the system.

It remains to explore how the PSF is altered in response to changes in the aberration function. The best image that can be produced is one that is diffraction limited (i.e. with no aberration), so that in the case of imaging a distant point source, the PSF is simply the modulus squared of the Fourier transform of the lens pupil function as given by Equation 25. With the addition of an aberration, the PSF is given by the modulus squared of the Fourier transform of the lens pupil function times the aberrated plane wave field. The additional phase distortions introduced by the aberration term give rise to increased image field intensities at the spatial frequencies contained in the aberration. Since total energy must be conserved, these increases in intensity must be accompanied by decreases in intensities at other locations. If the unaberrated PSF starts out as a single, strongly peaked function, we expect the increases in off-center intensities to come at the expense of the peak intensity.

As an example, consider a diffraction limited PSF dominated by a relatively narrow, central, single lobe of intensity. The aberrated PSF will have a wider central lobe, and new intensity lobes will be found away from the central lobe. In addition, the central peak intensity will be lower, as its energy is redistributed to the new off-center lobes. Since the lobes of the PSF will be getting broader, aberrated images of extended objects experience a loss of resolution, as the point spread functions produced by each point in the object
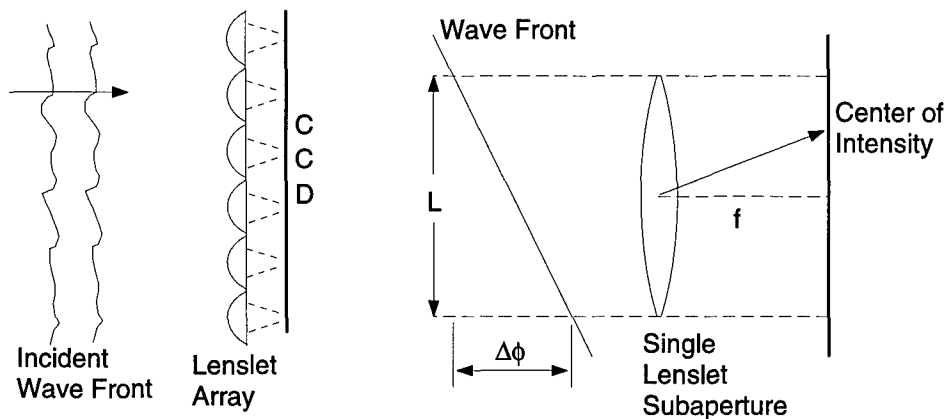
Figure 6.   Operation of a Hartmann WFS, due to Figure 5-6 from Roggemann and Welsh, *Imaging Through Turbulence*.

begin to overlap. This is best understood by interpreting the convolution operation of Equation 22 as a smoothing function. The more spread out a PSF is, the less fine detail will be evident in the resulting image after convolution with the "perfect" geometrical image.

This concludes the results from Fourier optics that are necessary for the developments in the rest of the thesis. The most important concepts developed were the Fourier transforming properties of lenses, the equivalency of the PSF to the focal plane image intensity of distant point sources, and the effects of aberrations on the PSF. With our Fourier optics tools in hand, the operation of a Hartmann WFS will be addressed using the developed framework.

2.4   Hartmann Wave Front Sensor

2.4.1   Model of Operation.   The Hartmann WFS is a device used to spatially sample the wave front slope of an incident field. As used in this research, it is physically comprised of two primary components: a lenslet array, and a charge coupled device (CCD) imager. The model configuration is depicted on the left side of Figure 6. The lenslet array is an array of square lenses of common focal length, bonded together to provide a means of segmenting an incident field into an array of focused images. The CCD imager is a pixel imaging system comprised of an array of solid state photo-detectors. The CCD array is

26

positioned behind the lenslets, at their focal length, so that the array of images is recorded for subsequent analysis.

To understand the operating principles behind the configuration, consider the scenario depicted on the right side of Figure 6. It depicts a single lenslet, focusing a small segment of the incident wave front. The incident wave front will have some average slope over the lenslet subaperture, and this is modeled by a plane wave, incident on the lenslet at the correct angle to equal the average slope of the actual wave front segment. With this model, the image produced on the CCD will be the diffraction pattern predicted by Equation 18 for the proper choice of $g_o(x, y)$ and $P(x, y)$. The remaining analysis will be performed in one dimension, rather than two, to simplify the calculations involved. The two-dimensional result will be a simple extension.

Before defining the correct functional form for the wave front in Figure 6, consider the following definition of the rectangle function:

$$\text{rect}(x) = \begin{cases} 1 & |x| < 1/2 \\ 0 & \text{elsewhere} \end{cases} \tag{30}$$

Then, the appropriate choices for the functions required to calculate the image produced by the scenario of Figure 6 are,

$$g_o(x) = \exp(isx) \tag{31}$$

$$P(x) = \text{rect}\left(\frac{x}{L}\right) \tag{32}$$

where L is the width of the square lenslet subaperture, and s is the slope of the optical field in radians per meter. The resulting image intensity on the CCD, I_i, is the square of the magnitude of the field predicted by Equation 18,

$$I_i(x) = |g_i(x)|^2 = \left(\frac{1}{\lambda f}\right)^2 \mathcal{F}\left\{e^{isx}\text{rect}\left(\frac{x}{L}\right)\right\}^2 \Bigg|_{f_x = \frac{x}{\lambda f}}$$

$$= \left(\frac{L}{\lambda f}\right)^2 \text{sinc}^2\left(L\left[\frac{x}{\lambda f} - \frac{s}{2\pi}\right]\right), \tag{33}$$

27
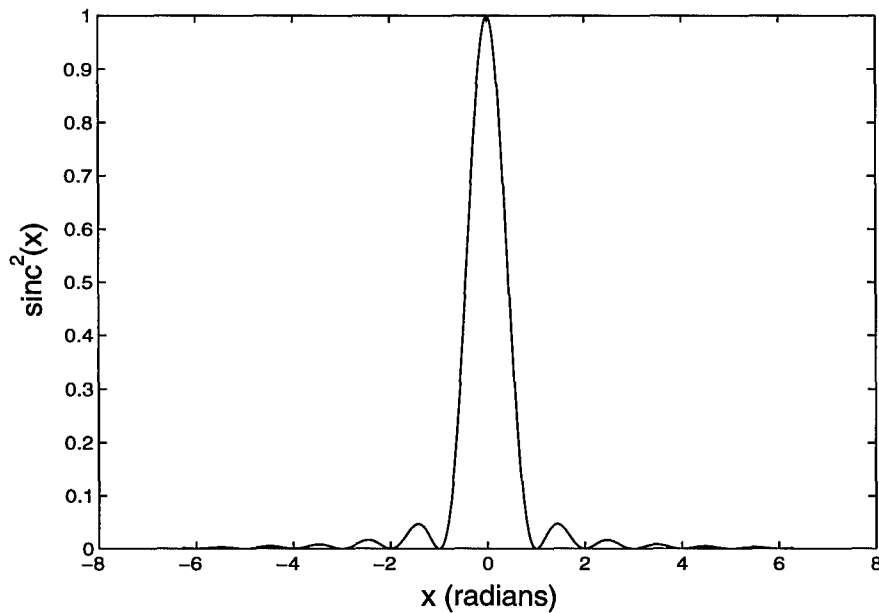
Figure 7. Plot of $\text{sinc}^2(x)$.

where the sinc function is defined by $\text{sinc}(x) = \dfrac{\sin(\pi x)}{\pi x}$. Examining the functional form of the intensity, specified by Equation 33, shows that it is a symmetric function centered at,

$$x_c = \frac{\lambda f}{2\pi} s. \tag{34}$$

A plot of $\text{sinc}^2(x)$, in Figure 7, shows the function to be strongly peaked about its center location. By locating x_c for a given subaperture, the slope across that subaperture will be given by solving Equation 34 for s,

$$s = \frac{2\pi}{\lambda f} x_c. \tag{35}$$

Thus, the position of the peak can be used to calculate the original slope of the wave front segment. In two dimensions, the intensity pattern consists of the product of two independent, one-dimensional sinc functions. Therefore, the measured slopes in each direction are independent of each other.

As an example of the type of shifts experienced in the intensity distribution, consider the normalized intensity profiles in Figure 8. The parameters of Equation 33 have been

28
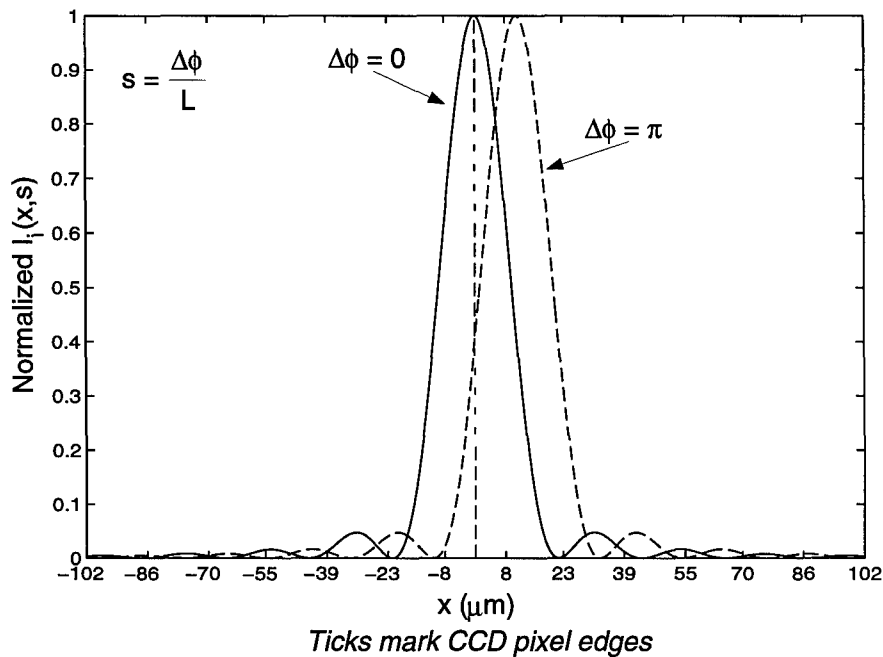
Figure 8. Plot showing the shift in intensity resulting from $\Delta\phi = 0$ and $\Delta\phi = \pi$ across the aperture.

chosen to reflect the actual dimensions used in the demonstration: $\lambda = 632.8$ nm, $f = 7$ mm, and $L = 203$ μm. For the solid curve, $s = 0$, while the dashed curve shows $s = \pi/L$, so that the change in phase is π across the subaperture. The x-axis tick marks have been chosen to show the edges of the pixels in the CCD array used to record the image. Each pixel is square, measuring 15.6 μm on a side. There are 13 pixels per subaperture dimension, and the subaperture is centered on the middle pixel. From the plot, we see that a π change in phase across the subaperture shifts the intensity peak into the pixel to the right of center. Of course, negative values of s would shift the peak in the negative x direction. Greater values of s will result in greater shifts in the peak center, until the edge of the aperture is reached.

The method employed by this research to calculate the peak center location from the recorded CCD image was an intensity centroid calculation, analogous to a mass centroid calculation. By weighting each CCD pixel location as the product of its intensity and distance from the center of the subaperture, the centroid of the intensity can be located

29
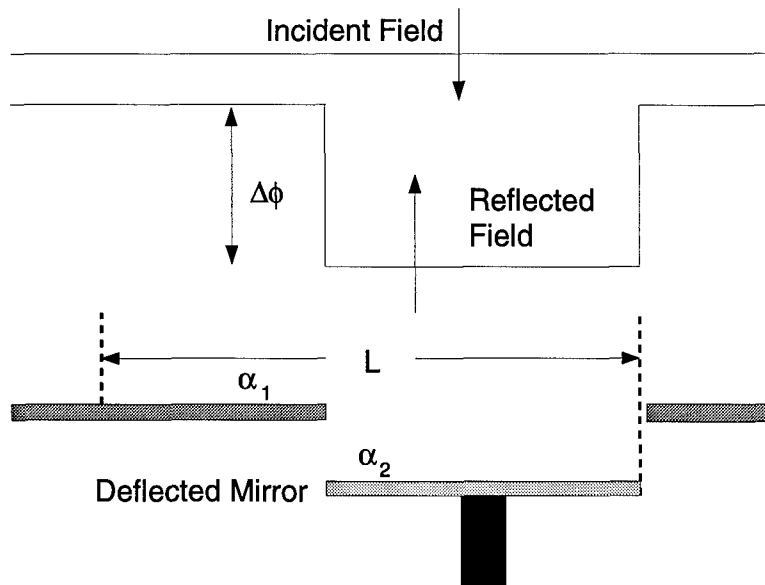
Figure 9. A single MEMS mirror deflecting and setting up a discontinuity in the reflected field.

with sub-pixel accuracy. By locating the intensity peak in the x- and y-directions, the slope of the wave front in both directions can be calculated by using Equation 35. This method will have low error for sharply peaked intensity distributions, like those indicated by Equation 33.

2.4.2 Measuring MEMS Reflections. As discussed in the introduction, the MEMS devices used for altering the phase of a wave front are piston devices. Thus, when a MEMS mirror deflects, it sets up a phase discontinuity in the reflected field, proportional to the distance between the mirror surface and the top of its surrounding posts, which may have different reflectivities. The situation can be modeled in one dimension as indicated in Figure 9, where a MEMS mirror has deflected relative to the post surfaces. Suppose the mirror and posts line up with a particular Hartmann subaperture, as indicated by the dashed lines of separation L in Figure 9. The actual field presented to the subaperture will have an average $\Delta\phi$, but it is not evident that the resulting intensity pattern focused onto the CCD will be what we expect.
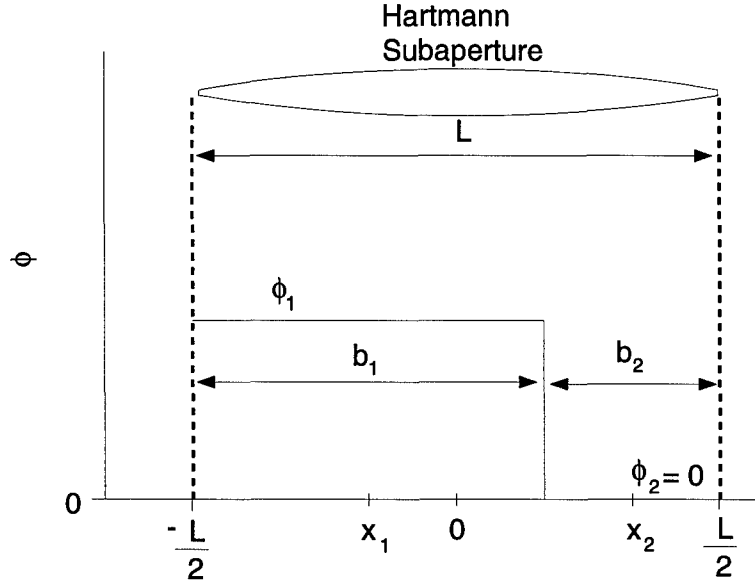
Figure 10. Model of reflected field phase incident on a Hartmann subaperture.

To find out, consider the model of the reflected field phase shown in Figure 10. Without a loss of generality, set $\phi_2 = 0$ and let ϕ_1 represent the $\Delta\phi$ in the reflection. The notation in Figure 10 is suggestive of a pair of rect functions with varying widths (specified by b_n) and center locations (specified by x_n). The optical field presented to the Hartmann subaperture is then,

$$g_o(x) = \alpha_1 e^{i\phi_1} \text{rect}\left(\frac{x - (b_1 - L)/2}{b_1}\right) + \alpha_2 \text{rect}\left(\frac{x - b_1/2}{L - b_1}\right), \qquad (36)$$

where we used $\phi_2 = 0$, $x_2 = b_1/2$, $x_1 = (b_1 - L)/2$, and $b_2 = (L - b_1)$. The reflectivity of each part of the MEMS is now contained in each α_n coefficient. The only independent dimensions are seen to be b_1 and L, the width of the post and subaperture, respectively.

To arrive at the field produced on the CCD array by the lenslet, apply Equation 18, as before, and arrive at,

$$\begin{aligned} g_f(x) &= \frac{e^{ikf} \exp\left[i\frac{k}{2f}\left(u^2 + v^2\right)\right]}{i\lambda f} \left[\alpha_1 e^{i\phi_1} e^{-i2\pi\frac{b_1 - L}{2\lambda f}x} b_1 \text{sinc}\left(\frac{b_1 x}{\lambda f}\right) + \right. \\ &\quad \left. \alpha_2 e^{-i2\pi\frac{b_1}{2\lambda f}x}(L - b_1)\text{sinc}\left((L - b_1)\frac{x}{\lambda f}\right)\right]. \end{aligned} \qquad (37)$$

The immediate effect to note is the result of setting α_1 or α_2 equal to zero (i.e. no reflection from that part of the MEMS). The intensity on the CCD is given by,

$$\alpha_1 = 0 \quad \Rightarrow \quad I_i(\alpha_1 = 0) = \left[\frac{\alpha_2(L - b_1)}{\lambda f}\text{sinc}\left((L - b_1)\frac{x}{\lambda f}\right)\right]^2, \tag{38}$$

$$\alpha_2 = 0 \quad \Rightarrow \quad I_i(\alpha_2 = 0) = \left[\frac{\alpha_1 b_1}{\lambda f}\text{sinc}\left(\frac{b_1 x}{\lambda f}\right)\right]^2. \tag{39}$$

Both cases result in intensities that are independent of ϕ_1! Since the peaks of the sinc^2 patterns won't shift in response to changes in mirror deflection, the Hartmann subaperture is incapable of measuring changes in the field reflected by the MEMS.

The situation is not much improved for the case where both surfaces have non-zero reflectivities. It can be shown that the general intensity on the CCD for non-zero reflectivities becomes,

$$
\begin{aligned}
I_i(x) \quad = \quad & \left[\frac{\alpha_1 b_1}{\lambda f}\text{sinc}\left(\frac{b_1 x}{\lambda f}\right)\right]^2 + \left[\frac{\alpha_2(L - b_1)}{\lambda f}\text{sinc}\left((L - b_1)\frac{x}{\lambda f}\right)\right]^2 + \\
& \frac{2\alpha_1\alpha_2 b_1(L - b_1)}{(\lambda f)^2}\text{sinc}\left(\frac{b_1 x}{\lambda f}\right)\text{sinc}\left((L - b_1)\frac{x}{\lambda f}\right)\cos\left(\frac{\pi L x}{\lambda f} - \phi_1\right). \quad (40)
\end{aligned}
$$

Only the cosine term in the expression has a dependence on ϕ_1. The first two terms provide a constant sinc pattern, firmly planted in the middle of the aperture and independent of the mirror deflection. The cosine term provides the only means to alter the intensity in response to changes in ϕ_1.

The top plot of Figure 11 shows the effect on the CCD intensity specified by Equation 40 of changing the wave front $\Delta\phi$ by adjusting ϕ_1 from zero to $\frac{2}{3}\pi$. The reflectivities were chosen to be equal and $\alpha_1 = \alpha_2 = 1$, and $b_1 = 0.3L$. The parameters L, λ, and f were chosen to reflect the actual values used in the demonstration, and are identical to those specified for Figure 8 (see page 29), so that the figures are directly comparable. The solid curve shows an intensity distribution for $\phi_1 = 0$ (no deflection of the mirror), and is the same as the solid curve in Figure 8, as we expect. The dashed curve shows the resulting intensity distribution when a discontinuity of $\phi_1 = \frac{2}{3}\pi$ is present in the reflected field. We see that the intensity peak has indeed shifted in the positive x-direction, but it has lost
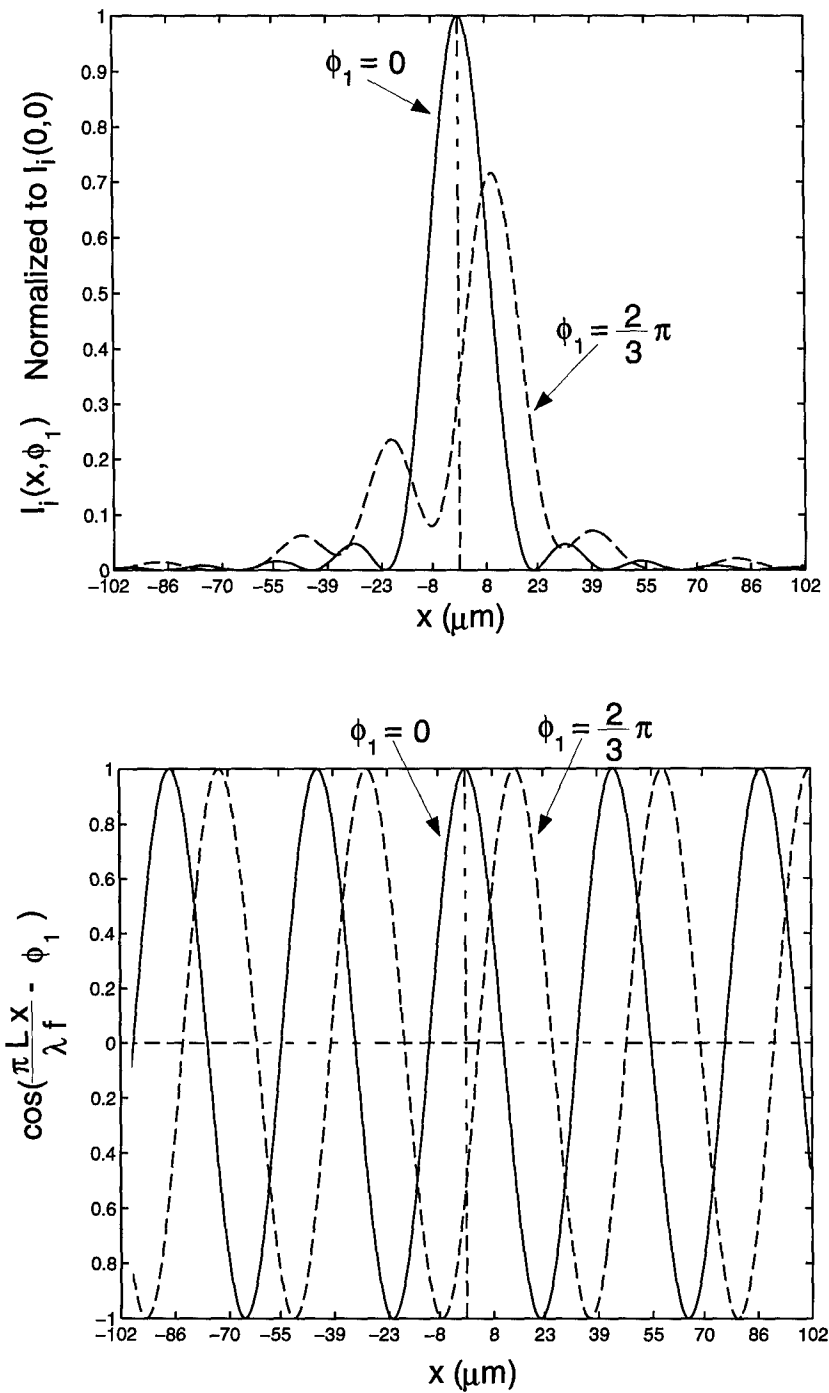
Figure 11.   Effect on intensity distribution of changing the phase discontinuity in the reflected field. The top plot shows the actual intensity profile for two cases. The bottom plot shows the effect of the same shift in phase on the cosine term of the intensity relation.
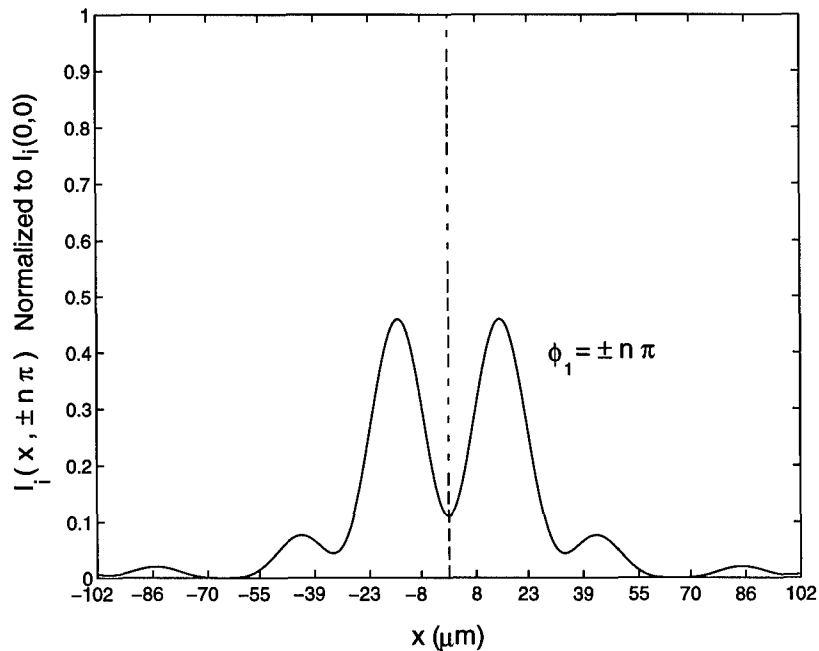
Figure 12. Intensity profile on CCD for $\phi_1 = \pm n\pi$. Note the symmetry of the peaks, resulting in a mean intensity location of zero.

intensity, while the off-center lobes have gained intensity. In particular, the lobe just to the left of the highest peak gains the most as the peak shifts in response to greater ϕ_1.

To gain some additional insight into the expected behavior of Equation 40, consider the bottom plot in Figure 11. It shows the phase shift of the cosine term in Equation 40 for the same change in ϕ_1 indicated in the top plot. ϕ_1 changes the phase of the cosine term, altering the distribution of weights it provides to its center-located, sinc multipliers. As ϕ_1 increases, the cosine applies mostly positive weights just to the right of center, and negative weights just to the left of center. The sinc multiplier terms fall off rapidly from their peak values, so the cosine's effects are dramatic only in the region around the center of the plot.

Since the cosine is a periodic function in phase, we would expect the weightings to repeat themselves as ϕ_1 progresses through multiples of $\pm\pi$. The maximum shift in the peak will occur for $\phi_1 = \pm n\pi$ (for integer n), and Figure 12 shows the resulting intensity profile. This situation shows the ambiguity of using the intensity centroid location to

34
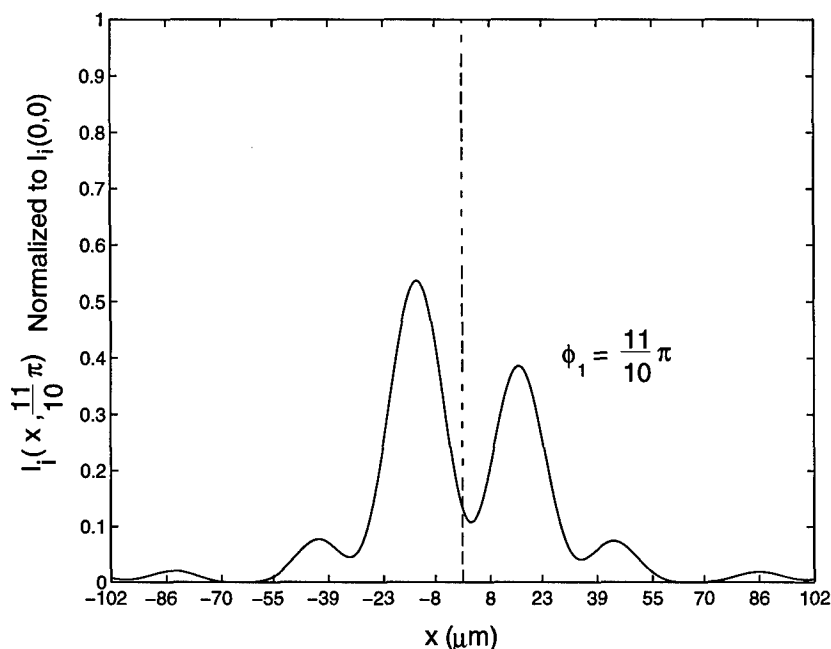
Figure 13.   Intensity profile on CCD for $\phi_1 = \frac{11}{10}\pi$. The resulting distribution is indistin-guishable from a negative value of the ϕ_1.

compute the resulting average slope across the subaperture. Clearly, the location of the intensity centroid is $x = 0$ for this symmetric curve, which would indicate an average slope of zero, when in fact it is some multiple of π. In addition, the maximum shift in the peaks only puts each peak in the CCD pixel location immediately adjacent to zero.

Figure 13 shows the effect of increasing ϕ_1 just past π to $\frac{11}{10}\pi$. The resulting intensity profile resembles a negative ϕ_1. In addition, the computed centroid of the intensity will be close to zero, since the peak to the right of $x = 0$ is just slightly less than the highest peak.

To demonstrate the difficulty in using the intensity centroid to determine s, as we did using Equation 35 for the plane wave case, consider the plot of intensity centroid location as a function of ϕ_1, shown in Figure 14. To generate the plot, the centroid of the intensity, x_c, was calculated for the intensity distribution given by Equation 40 as ϕ_1 varied. The parameters L, f, and λ were set to the values actually used in the demonstration, and were specified on page 29. The reflectivities were chosen $\alpha_1 = \alpha_2 = 1$, while $b_1 = 0.3L$.

35
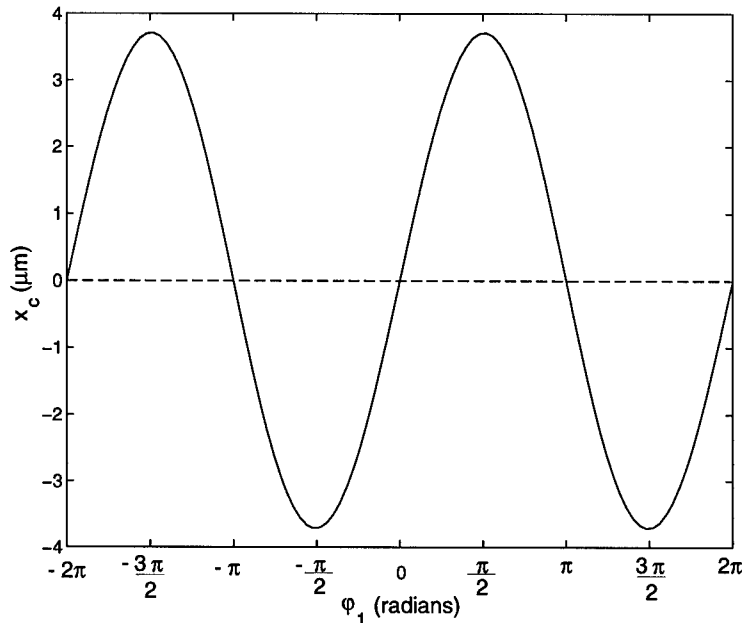
Figure 14.   Location of intensity centroid, x_c, as a function of ϕ_1, the discontinuity in the MEMS reflected field.

Thus, the results in Figure 14 contain the actual intensity centroid locations for Figures 11, 12, and 13. As would be done using actual CCD data, the peak intensity was calculated by an intensity centroid method. We clearly see the periodic nature of the location of the intensity centroid as ϕ_1 changes. Unfortunately, we cannot unequivocally derive the incident average slope across the subaperture from such a calculation, as we did for the plane wave case.

These plots have conveyed the difficulty in using an intensity centroid method to infer a change in average slope across the Hartmann subaperture for discontinuous fields. Changes in $\Delta\phi$ merely redistribute energy from the central peak to off-center lobes, rather than inducing a uniform shift in the intensity pattern. Most importantly, the intensity patterns are inherently periodic, and there is no way to distinguish between slopes that differ by multiples of π.

The effects of changing the values of the parameters in Equation 40 could be further explored, but the fundamental problems will remain. For this thesis, the important result is

that a Hartmann sensor is not appropriate for general use in measuring the fields reflected by a MEMS mirror array. The only solution to the situation seems to be to choose a geometry such that many MEMS mirrors are contained in each Hartmann subaperture, so that the field across the subaperture has small discontinuities at each plateau. This will result in a closer approximation to a linear phase change for the field within each subaperture. However, this requires many MEMS mirrors for a significant number of Hartmann subapertures to be employed. The MEMS mirror arrays currently available did not have enough mirrors to allow for more than a few mirrors per subaperture while still employing a significant number of subapertures.

2.5 Wave Front Reconstruction

The previous section showed the method by which a Hartmann WFS can be used to spatially sample a wave front and generate slope measurements. This section will address how to use the slope measurements to reconstruct an estimate of the original wave front phase. Perfect knowledge of the original phase is impossible, so we must settle for a representation that suits our needs.

The wave front phase that reaches the Hartmann will be represented by $\phi(\vec{x})$. The goal of this development is to arrive at a representation of $\phi(\vec{x})$ as a sum of appropriately weighted elementary basis functions. The estimator, $\tilde{\phi}(\vec{x})$, of the wave front phase is to be of the form [1:251],

$$\tilde{\phi}(\vec{x}) = \sum_{i=1}^{I} c_i e_i(\vec{x}), \qquad (41)$$

where $e_i(\vec{x})$ are the elementary functions chosen for the basis set, and c_i are the weights to be calculated by the reconstruction method. I is the number of elementary functions in the basis set. The elementary functions can be any suitable set of functions defined in the pupil of the Hartmann sensor. Examples include sets of shifted exponentials, triangle functions, sinc functions, or the Zernike polynomials [1:94–98]. The choice of c_i's is really a linear least-squares fitting problem, as will be demonstrated shortly by selection of a measure of error for $\tilde{\phi}(\vec{x})$ and subsequent minimization of that error to determine the c_i's.

The only information available to calculate c_i are the slope measurements, $\vec{s}_m(k)$, where k numbers the Hartmann lenslet array in row major format. Since the Hartmann produces an x- and y-direction slope measurement for each subaperture, $\vec{s}_m(k)$ will have two components, represented by the scalars $s_m^x(k)$ and $s_m^y(k)$, such that,

$$\vec{s}_m(k) = s_m^x(k)\hat{x} + s_m^y(k)\hat{y}, \tag{42}$$

where $\hat{x}$ and $\hat{y}$ are unit vectors in the designated direction. k can have a value from 1 to the maximum number of subapertures, K. We wish to order the slope measurements in a single column vector so that a consistent matrix notation can be employed in subsequent analysis. This column vector will be length $J = 2K$, and the ordering scheme will be [1:252],

$$
\begin{aligned}
s_m(1) &= s_m^x(1), \\
s_m(2) &= s_m^y(1), \\
s_m(3) &= s_m^x(2), \\
s_m(4) &= s_m^y(2), \\
&\quad\vdots \\
s_m(J-1) &= s_m^x(K), \\
s_m(J) &= s_m^y(K).
\end{aligned} \tag{43}
$$

The column vector s_m is numbered by j and now contains all the Hartmann slope measurements.

We choose to derive a relationship between c_i and $s_m(j)$ such that [1:252],

$$\mathbf{c} = \mathbf{M}\,\mathbf{s_m}, \tag{44}$$

where $\mathbf{M}$ is a matrix of I rows and J columns, each element represented by M_{ij}. $\mathbf{c}$ and $\mathbf{s_m}$ are both column vectors composed of elements given by c_i and $s_m(j)$, respectively.

To proceed, we need to calculate the elements of $\mathbf{M}$ such that the $\mathbf{c}$ elements produce a $\tilde{\phi}(\vec{x})$ that matches the original phase as closely as possible. We can choose a measure of error, ε, between $\tilde{\phi}(\vec{x})$ and $\phi(\vec{x})$ to indicate how closely our estimate matches the original phase at a given point. Then, by minimizing this error over the entire Hartmann aperture, we can arrive at an $\mathbf{M}$ that results in the best choices of c_i for a given $\mathbf{s_m}$.

The measure of error we choose is the squared difference between the measured slope and the slope produced by our estimator, $\mathbf{s_e}$. This will result in a least-squares minimization method for the calculation of $\mathbf{c}$. In particular, we choose to minimize,

$$\varepsilon^2 = |\mathbf{s_m} - \mathbf{s_e}|^2, \tag{45}$$

where the $j = 1 \ldots 2K$ elements of $\mathbf{s_e}$ are given by the average wave front phase gradient of $\tilde{\phi}(\vec{x})$ over the k-th Hartmann subaperture. As an intermediate step to calculating $\mathbf{s_e}$, consider calculating the overall slope vector $\vec{s}_e(k)$ of $\tilde{\phi}(\vec{x})$ for the k-th subaperture. This results in [1:183],

$$\vec{s}_e(k) = \int W_{sk}(\vec{x}) \nabla \tilde{\phi}(\vec{x}) d\vec{x}, \tag{46}$$

where $W_{sk}(\vec{x})$ is the pupil function for the k-th Hartmann subaperture. Note that $W_{sk}(\vec{x})$ is normalized so that,

$$\int W_{sk}(\vec{x}) d\vec{x} = 1. \tag{47}$$

Integrating Equation 46 by parts, we arrive at [31],

$$\vec{s}_e(k) = -\int \nabla W_{sk}(\vec{x}) \tilde{\phi}(\vec{x}) d\vec{x}, \tag{48}$$

so that the gradient operator is now acting on $W_{sk}(\vec{x})$. The gradient operator is composed of an x- and a y-component, so that the slope in a particular direction may be calculated by [1:125],

$$s_e^q(k) = -\int \nabla^q W_{sk}(\vec{x}) \tilde{\phi}(\vec{x}) d\vec{x}, \tag{49}$$

where q represents either x or y.

39

Substituting into Equation 49 our expression for $\tilde{\phi}(\vec{x})$ from Equation 41, we see [1:192],

$$s_e^q(k) = -\sum_{i=1}^{I} c_i \int \nabla^q W_{sk}(\vec{x}) e_i(\vec{x}) d\vec{x}. \tag{50}$$

Following the same ordering scheme developed in Equation 43, we can define a new function $Q_{sj}(\vec{x})$ as,

$$
\begin{aligned}
Q_{s1}(\vec{x}) &= \nabla^x W_{s1}(\vec{x}), \\
Q_{s2}(\vec{x}) &= \nabla^y W_{s1}(\vec{x}), \\
&\quad\cdot \\
&\quad\cdot \\
&\quad\cdot \\
Q_{s(J-1)}(\vec{x}) &= \nabla^x W_{sK}(\vec{x}), \\
Q_{sJ}(\vec{x}) &= \nabla^y W_{sK}(\vec{x}),
\end{aligned}
\tag{51}
$$

so that,

$$s_e(j) = -\sum_{i=1}^{I} c_i \int Q_{sj}(\vec{x}) e_i(\vec{x}) d\vec{x}, \tag{52}$$

produces a correctly ordered s_e for use in Equation 45. Equation 52 can be rewritten in matrix notation as [1:192],

$$\mathbf{s_e} = \mathbf{Hc}, \tag{53}$$

where the elements of $\mathbf{H}$ are defined by,

$$H_{ji} = -\int Q_{sj}(\vec{x}) e_i(\vec{x}) d\vec{x}. \tag{54}$$

Substituting Equation 53 into Equation 45,

$$\varepsilon^2 = |\mathbf{s_m} - \mathbf{Hc}|^2. \tag{55}$$

The squared error now directly relates the quantities we measure ($\mathbf{s_m}$) to the quantities we wish to calculate ($\mathbf{c}$). The goal is to minimize this error with respect to $\mathbf{c}$. Expanding Equation 55, taking the derivative with respect to $\mathbf{c}$, setting the derivative equal to zero,

and solving for **c** shows that [31],

$$\mathbf{c} = \left(\mathbf{H}^T\mathbf{H}\right)^{-1}\mathbf{H}^T\mathbf{s_m}, \tag{56}$$

will be the least-squares choice of **c** for the given $\mathbf{s_m}$. The T superscript designates the matrix transpose operator, and the -1 superscript is a matrix inversion. Comparing to Equation 44, we identify [1:253],

$$\mathbf{M} = \left(\mathbf{H}^T\mathbf{H}\right)^{-1}\mathbf{H}^T, \tag{57}$$

and the stated goals of this section are complete: we now have a matrix **M** that relates $\mathbf{s_m}$ to **c**, and we can generate the wave front estimator $\tilde{\phi}(\vec{x})$ in Equation 41.

The only task left is to further develop the form of H_{ji} given by Equation 54. To proceed, an expression for the k-th subaperture pupil function, $W_{sk}(\vec{x})$, is required. For the square apertures used by this research, the appropriate function is,

$$W_{sk}(\vec{x}) = \frac{1}{L^2}\text{rect}\left(\frac{x - x_{ck}}{L}\right)\text{rect}\left(\frac{y - y_{ck}}{L}\right), \tag{58}$$

where x_{ck} and y_{ck} represent the center location for the k-th subaperture, and L is the subaperture side dimension.

To evaluate $Q_{sj}(\vec{x})$, apply each component of the gradient operator to Equation 58 and reference the ordering scheme in Equation 51 to show [1:251],

$$\begin{aligned}
Q_{s(2k-1)}(\vec{x}) &= \nabla^x W_{sk}(\vec{x}) \\
&= \frac{1}{L^2}\left[\delta\left(x - x_{ck} + L/2\right) - \delta\left(x - x_{ck} - L/2\right)\right]\text{rect}\left(\frac{y - y_{ck}}{L}\right), \tag{59} \\
Q_{s(2k)}(\vec{x}) &= \nabla^y W_{sk}(\vec{x}) \\
&= \frac{1}{L^2}\left[\delta\left(y - y_{ck} + L/2\right) - \delta\left(y - y_{ck} - L/2\right)\right]\text{rect}\left(\frac{x - x_{ck}}{L}\right). \tag{60}
\end{aligned}$$

41

Then, substituting into Equation 54, and recalling that that the j and k limits are related by $J = 2K$, the expressions for H_{ji} become,

$$H_{ji}(j \text{ even}) = -\frac{1}{L^2} \int \text{rect}\left(\frac{y - y_{cj}}{L}\right) \left[e_i\left(x_{cj} - \frac{L}{2}, y\right) - e_i\left(x_{cj} + \frac{L}{2}, y\right)\right] dy \quad (61)$$

$$H_{ji}(j \text{ odd}) = -\frac{1}{L^2} \int \text{rect}\left(\frac{x - x_{cj}}{L}\right) \left[e_i\left(x, y_{cj} - \frac{L}{2}\right) - e_i\left(x, y_{cj} + \frac{L}{2}\right)\right] dx \quad (62)$$

We see that the effect of the $Q_{sj}(\vec{x})$ term inside the integral is to have the δ-functions effectively transform Equation 54 into a one-dimensional integral that evaluates the elementary functions along the edges of a subaperture.

Some important insights and intuition can be developed from the expressions for H_{ji} in Equations 61 and 62. If a particular basis function has the same value along opposite edges of an aperture, it results in a zero H_{ji} element, i.e. it will be unconstrained by the slope measured by the subaperture. This presents some difficulties in choosing an appropriate set of basis functions for use as the $e_i(\vec{x})$. If we choose symmetric basis functions centered on each subaperture, then we will end up with no solution to Equation 56, since every basis function will be unconstrained. What we require is a set of basis functions where each function in the set is anti-symmetric across at least one subaperture. Then, it will be constrained by at least one slope measurement and a solution for the c_i may exist.

Since we have $2K$ slope measurements from the Hartmann sensor (an x- and y-direction measurement for each subaperture), we cannot use more than $I = 2K$ elementary functions in our basis set. We cannot require more unknowns than knowns. Another difficulty is that certain sets of basis functions cause $\left(\mathbf{H}^T\mathbf{H}\right)$ to become ill-conditioned, so that the inverse fails to exist, as required by Equation 56 [1:253].

This concludes the development of the theory of wave front reconstruction from slope measurements. We have shown that by calculating the H_{ji} elements through Equations 61 and 62, we can calculate a matrix $\mathbf{M}$ that allows us to generate a $\mathbf{c}$ vector based on the measured slopes in $\mathbf{s_m}$. The c_i are used to generate an estimate $\tilde{\phi}(\vec{x})$ to the wave front using a set of basis functions $e_i(\vec{x})$, as specified in Equation 41.

As outlined in the introduction, the approach to using a deformable mirror to correct an aberration is to match the mirror elements to the measured wave front phase aberration. The developments to this point have left us with a phase representation to use in determining what deflection each mirror should have to match the measured phase. The final piece required is a control law to determine what voltage to apply to achieve the desired deflection in a particular mirror. The next section presents the derivation of the applicable control law.

2.6 MEMS Control Theory

Developing and validating a precise model of the theoretical response of a MEMS mirror as a function of an applied voltage is a complicated endeavor [9]. Michalicek showed that the response can be closely approximated by a simple relation if some assumptions are made [32]. For this development, the mirror is assumed flat, with no sagging due to gravity or electrostatic forces, and we assume electric field fringing effects at the edges of the mirror are negligible. Figure 15 is a SEM image of a single MEMS mirror, and Figure 16 shows the operational representation of the mirror used by the model. In the model, the flexure beams are characterized as simple springs, where the restoring force is linearly related to the deflection of the mirror by a constant, k. The mirror has area A, and a voltage V is applied between the mirror and the address electrode.

The geometry used to specify the forces on the mirror is shown in Figure 17. z_0 is the distance from the mirror's resting position to the address electrode on the substrate, d_f is the deflection induced on the mirror, and z_m is the deflected mirror's distance from the electrode.

Then, the force F_v on the mirror from the applied voltage is given by a simple electrostatic relationship as [32],

$$
\begin{aligned}
F_v &= \frac{\epsilon_0 \left(V/z_m\right)^2}{2} A, \\
&= \frac{\epsilon_0 A}{2} \left[\frac{V}{(z_0 - d_f)}\right]^2,
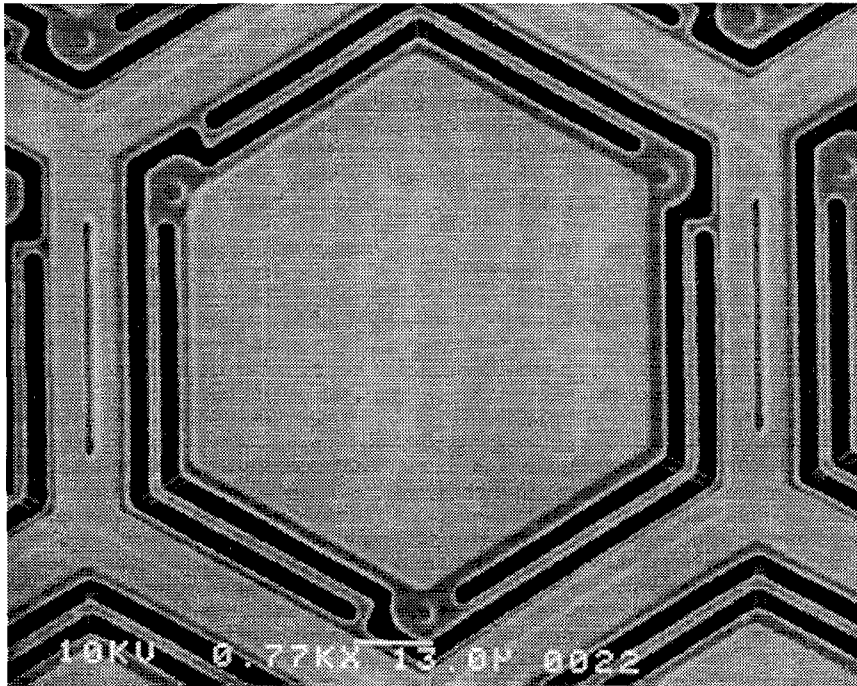\end{aligned}
\tag{63}
$$

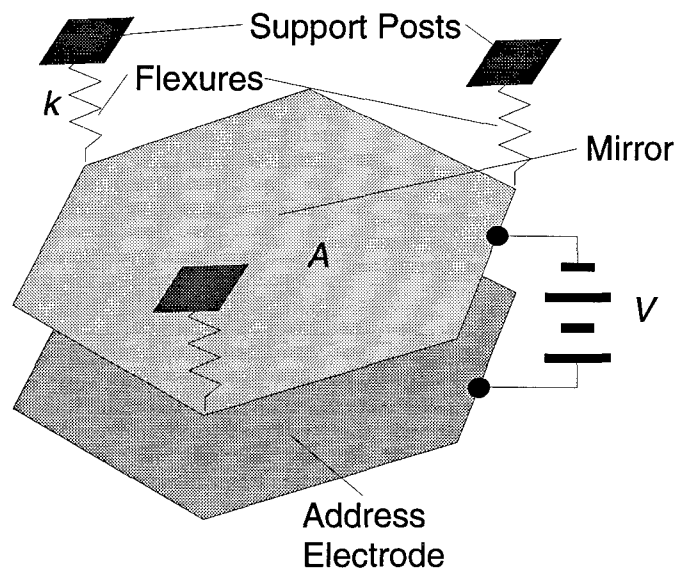Figure 15. SEM micrograph of a single MEMS mirror.

Figure 16.   The modeled representation of a single mirror used to derive the response of
the mirror to an applied voltage. The parameters indicated are voltage (V),
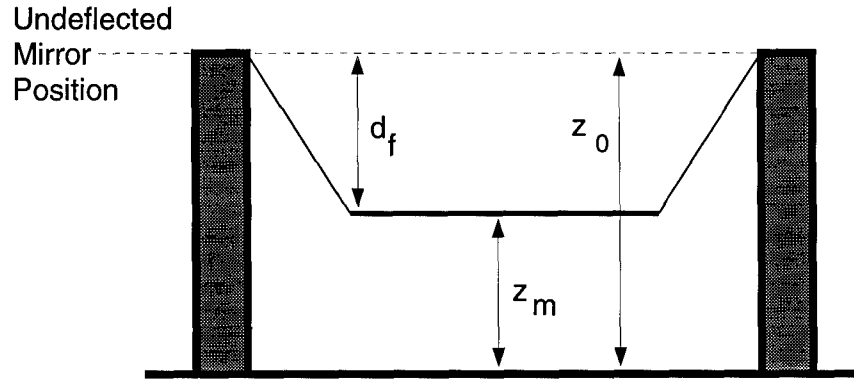area of the mirror (A), and spring constant (k).

44

Figure 17. The variables used to describe the deflection of a single MEMS mirror.

where ϵ_0 is the permittivity of free space, used as an approximation to the permittivity of air. The second line has substituted $z_m = (z_0 - d_f)$ from the problem geometry.

The subsequent restoring force on the mirror from the flexure arms is given by Hook's law,

$$F_f = k d_f. \tag{64}$$

At equilibrium, the two forces balance. Setting $F_v = F_f$ and solving for V as a function of d_f, we see [32],

$$V = (z_0 - d_f) \sqrt{\frac{2k d_f}{\epsilon_0 A}}. \tag{65}$$

In the above relation, A and z_0 are known from the fabrication parameters of the design. $\epsilon_0 \approx 1$, and k can be derived theoretically from various material properties [32]. However, if a new constant $\hat{k}$ is defined by,

$$\hat{k} = \sqrt{\frac{2k}{\epsilon_0 A}}, \tag{66}$$

then the voltage relation in Equation 65 becomes,

$$V = \hat{k} (z_0 - d_f) \sqrt{d_f}. \tag{67}$$

$\hat{k}$ can be determined experimentally by measurement of a V and d_f pair.

Equation 67 suits our needs perfectly: we will be calculating required deflections, d_f, for individual mirrors from our wave front reconstruction of the aberrated phase. Equa-

45

tion 67 will then give us the required voltage to apply to a mirror to achieve the desired deflection.

This concludes the theoretical developments necessary for the rest of the thesis. The next chapter discusses the experiment design and methodology used to perform the demonstration.

III. Experiment Methodology

3.1 Chapter Overview

This chapter presents the experimental arrangement, components, and procedures used to perform the demonstration. Before discussing the actual setup, a brief overview of the entire demonstration is provided. Then, the experimental setup is covered by component, with more detailed discussions on the critical features of the design. The last section contains a discussion of each step in demonstration to show the procedures used.

3.2 Overview of Demonstration

The goal of this research was to demonstrate the use of an available MEMS micromirror array to correct a static optical aberration. It was not expected that complete correction of an aberration could be achieved with the devices available [28]: the degree of success was to be determined by the research. Thus, data was required that could be used to characterize the performance of the MEMS as a deformable mirror.

To simulate astronomical imaging conditions, the setup was designed to image planar wave fronts after reflection from the MEMS. The key measure of performance was the point spread function (PSF) of the focused MEMS reflection. As established in Section 2.3, the PSF for our system is equivalent to the intensity distribution of the far-field diffraction pattern of the reflection. The differences in the PSF characteristics between an aberrated and unaberrated wave front were discussed in Section 2.3. An improved PSF is one that is higher and narrower in its central lobe. Off-center lobes should decrease in intensity as the aberration is improved.

The demonstration started by using a plane wave for reference measurements, and then using a long focal length lens to introduce a slight, spherical aberration to the plane wave. The resulting aberration was measured with a wave front sensor, and appropriate voltages were calculated to match the MEMS shape to the aberration. By focusing the MEMS reflections, the corrected and uncorrected PSF intensity distributions were measured and compared. The following section details the final configuration of the experimental setup used to take the required measurements.

47

3.3 Setup and Components

Any experimental setup must be designed for the measurements that are necessary. An outline of the required measurements for this demonstration is presented below. Each measurement gives rise to design issues that must be accounted for in the experimental setup. By no means did all the design issues become apparent before the first measurements were taken. The experimental design was an iterative process, and the discussion here is meant to reflect the final state of the demonstration.

- **Reference PSF intensities**

  In general, a method of recording PSF intensity distributions was required. In particular, we required reference PSF measurements for plane wave reflections off of a plane mirror and the MEMS device. These reference reflections served two purposes. The first was to provide a benchmark to which the aberrated reflections could be compared. The second purpose was to use the planar reference reflection to determine the subsequent aberration put into the system by addition of the aberrating lens.

- **Aberrated phase**

  A method was required by which the aberrated wave front phase could then be measured without disturbing the rest of the setup. As discussed in Section 2.4, using a Hartmann WFS to measure wave front phases from MEMS reflections is not generally appropriate. Thus, a key design parameter was to allow the measurement of the aberration to occur without the MEMS mirror array in the beam path.

- **Uncorrected PSF**

  With the MEMS mirror elements in an undeflected position, the PSF of the aberration was measured after reflection from the MEMS.

- **Corrected PSF**

  The final step was to deflect the MEMS mirrors to correct the aberration and measure the resulting PSF. The setup was designed to allow for flexibility in controlling the MEMS mirror deflections so that the exact nature of the aberration was not critical to the success of the demonstration.

Lens Label		Focal Length
Collimating	f_c	200 mm
Aberrating:	f_{a1}	-500 mm
Component	f_{a2}	175 mm
Focal Lengths	f_{a3}	-250 mm
Combined Aberrating	f_a	-3.5 m
LP_M	f_{M1}	88.3 mm
	f_{M2}	15.36 mm
LP_P	f_P	100 mm
LP_T	f_T	300 mm
$L_{\mathcal{F}}$	$f_{\mathcal{F}}$	62.90 mm
L_{Mag}	f_{Mag}	11 mm

Table 1. Focal lengths of lenses used in experimental setup.

With these design issues in mind, the experimental setup depicted in Figure 18 was used to accomplish the required measurements. Table 1 provides the focal lengths of the lenses used in the setup. A detailed description of the use and placement of each component will be described in the following pages, but the critical separation distances have been indicated in the figure. In summary, the indicated lens pairs formed afocal imaging systems, thus they were separated by the sums of their focal lengths: LP_T and LP_P were non-magnifying, while LP_M magnified the MEMS by a factor of 5.75. The MEMS, the plane mirror at the bottom of the figure, the WFS, and $L_{\mathcal{F}}$ were all placed in the back focal plane of their respective lens pair, consistent with the requirements of an afocal imaging system. The front focal planes of LP_M and LP_P coincided just past the aperture, as indicated by the dashed line in front of the aperture. This ensured that the MEMS and plane mirror reflected the same incident field. Furthermore, the imaging focal planes of LP_M and LP_P coincided with the front focal plane of LP_T, as indicated by the dashed line between the labeled beam splitter and the first lens of LP_T. This ensured that the subsequent reflected field was imaged by LP_T immediately after reflection from both surfaces. $L_{\mathcal{F}}$ provided the PSF (equivalent to the far-field diffraction pattern) at its back focal plane, which was then imaged by L_{Mag}. The CCD was adjusted in position relative to L_{Mag} to control the magnification of the resulting PSF intensity distributions.
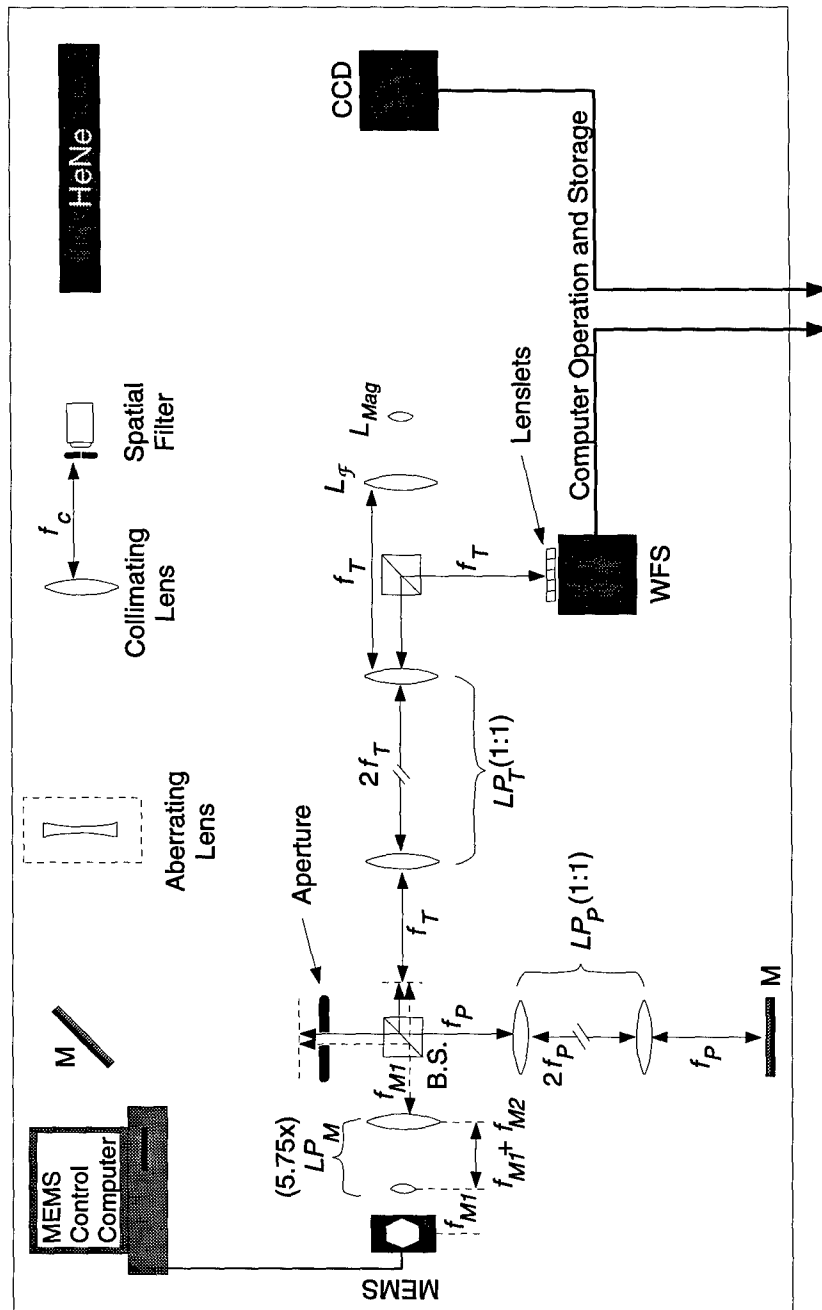
Figure 18. A depiction of the lab bench experimental setup. Component labels are **M** (Mirror), **B.S.** (Beam Splitter), **CCD** (Charge Coupled Device Imager), **WFS** (Hartmann Wave Front Sensor), LP_M (MEMS Lens Pair), LP_P (Plane Mirror Lens Pair), LP_T (Translating Lens Pair), $L_{\mathcal{F}}$ (Focusing Lens), L_{Mag} (Magnifying Lens). LP_T and LP_P are non-magnifying, afocal imagers, while LP_M is an afocal imager magnifying the MEMS array by 5.75X.

All components were mounted on an optical lab bench that was vibration isolated through a pneumatic suspension system. For all measurements, a 1 mm diameter, 18 mW Helium-Neon (HeNe) laser beam was passed through a spatial filter and collimating lens. The spatial filter consisted of a microscope objective and 15 μm pinhole. After the spatial filter, the beam was allowed to expand to a large size before being collimated by a lens of focal length $f_c = 200$ mm. The large beam waist at the collimating lens ensured that the propagating optical field would not depart measurably from a planar wave front within the dimensions of the optical bench.

The aberrating lens was post mounted and added to the setup only after the planar reference measurements were taken. The long focal length desired for the aberrating lens required the use of three shorter focal length lenses in combination (see Table 1). For tracing the beam path, the presence of the aberrating lens is irrelevant. For the rest of the setup discussion, we will simply refer to the "wave front" of the optical field and make the distinction between aberrated and unaberrated wave fronts only when necessary.

After reflection from a plane mirror (at the top of Figure 18), the wave front encountered a circular iris. Small diameter beams were useful for aligning components, while for measurements, the aperture could be adjusted to expose only the MEMS mirror elements of interest. The beam splitter after the aperture sent the wave front on two separate paths, one for a MEMS reflection and one for a plane mirror reflection at the bottom of Figure 18. Since only one path was of interest for a given measurement, the other path was covered with a black, absorbing cloth when not in use.

First, consider the beam path shown in Figure 19, where the MEMS path has been covered and the beam path has been explicitly shown. Following the solid arrow, the wave front was imaged onto the plane mirror by a lens pair, LP_P. The lenses had equal focal lengths, f_P, and were separated by a distance of $2f_P$, resulting in a non-magnifying, afocal imaging system. Thus, the field reflected by the plane mirror was the same field located in the front focal plane of the first lens. The lenses were positioned so that they imaged the field just after the adjustable aperture.
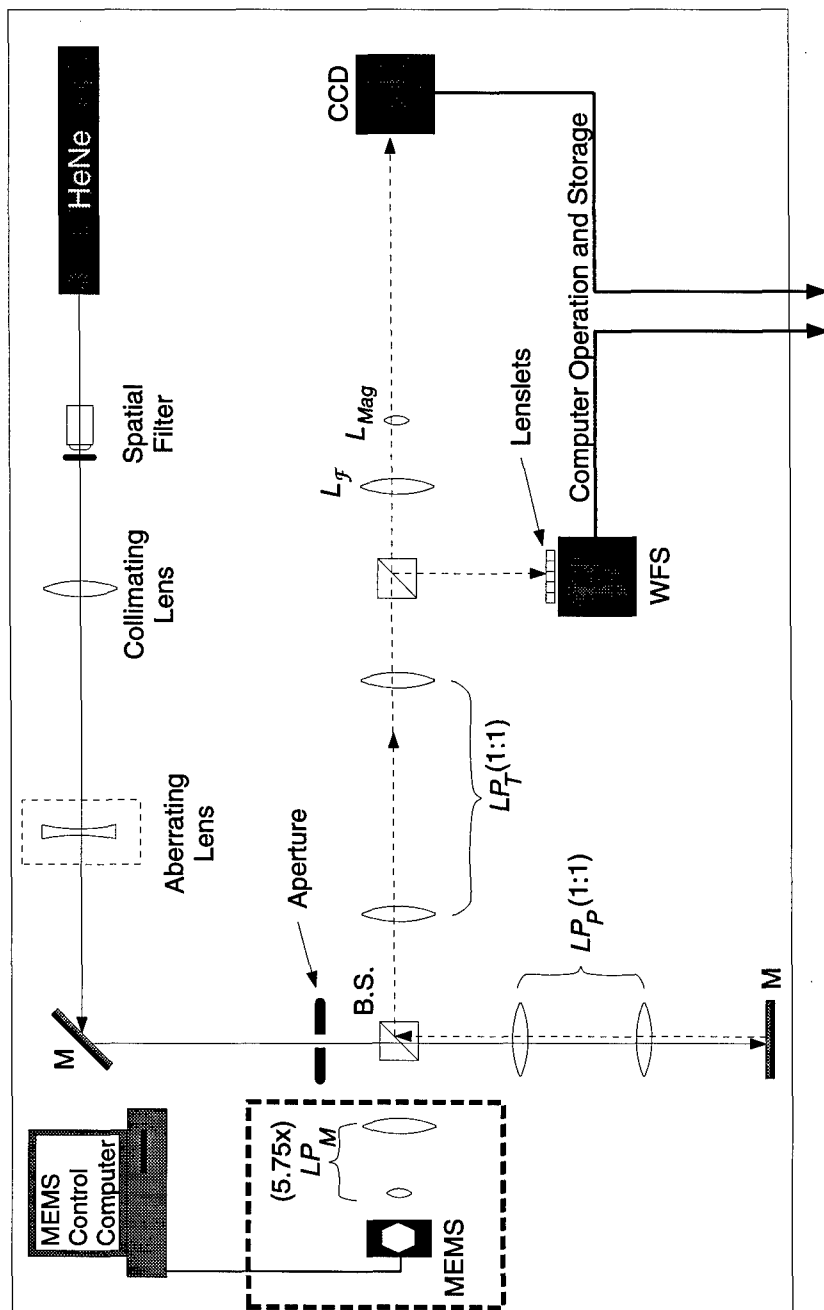
51

Figure 19. The beam path for plane mirror reflection measurements. The PSF is recorded by the CCD, while the WFS records the lenslet image for subsequent slope calculations. Without the aberrating lens, a reference PSF and wave front measurement can be taken. When the aberrating lens is added, the wave front measurement will be used to compute the resulting aberrated phase, and an aberrated PSF can be recorded for comparison.

Lenslets (ea.)	
Focal length	7 mm
Dimensions	203 μm, square
CCD	
Manufacturer	EG&G Reticon
Model	MD4256C
Pixels	256 x 256
Dimensions	4.1 mm, square

Table 2. Selected Hartmann sensor parameters.

The plane mirror was aligned normal to the incidence of the wave front, and it reflected the field back on itself along the return path indicated by the dashed arrow. After encountering the beam splitter, the field was partially reflected towards the lens pair, LP_T. The lenses had the same focal length, f_T, and formed another afocal, non-magnifying imaging system. They were positioned so that the focal planes of LP_P and LP_T coincided, resulting in an image field in the back focal plane of LP_T that was the field just after reflection from the plane mirror.

At the next beam splitter, two separate paths were taken by the field towards the measurement devices indicated. The reflected path was towards the WFS. Table 2 lists selected parameters for the Hartmann sensor elements. The lenslets of the sensor were positioned in the back focal plane of LP_T, so that the slopes measured by the WFS were for the field just after reflection from the plane mirror. In turn, the CCD used to record the resulting image was positioned at the focal length of the lenslets. The dimensions of the lenslets and CCD resulted in a 20 x 20 array of subapertures for the Hartmann WFS measurements. Each subaperture was comprised of a square array of 13 x 13 pixels in the resulting CCD image.

Along the non-reflected path, a focusing lens, $L_{\mathcal{F}}$, was placed at the back focal plane of LP_T, to image the reflected field. Another lens, L_{Mag}, was used to magnify the resulting image for the CCD array on the right end of Figure 19. The images recorded were the magnified PSF intensities for the plane mirror reflections. By adjusting the distance between the CCD and L_{Mag}, different magnifications of the PSF on the CCD were achieved. By positioning the CCD approximately 50 cm away from L_{Mag}, the PSF

could be magnified to the point that the central order filled about 25 percent of the CCD aperture. The CCD array was the same type used to record the Hartmann WFS data.

Both CCD arrays were driven by their own IBM compatible computer and software. The computer interface displayed real-time intensity images for general viewing and alignment. The CCD cameras could be operated at variable frame rates, ranging from 1 to 1000 frames/sec, allowing for changes in integration times to compensate for low or high intensity images. Approximately 500 frames at a time were stored in computer memory during real time viewing, with new frames constantly overwriting old frames as the buffer filled. By suspending real time viewing, selected frames from the buffer could be stored to disk in a raster format for subsequent analysis. The values stored were intensity values for each CCD pixel, ranging from zero to 255 in integer increments (eight bit, unsigned integer storage).

Returning to the MEMS reflection path, Figure 20 shows the beam path for measurements involving MEMS reflections. Following the solid arrow from the beam splitter, we see the field encountered the LP_M lens pair. The lens pair focal lengths were chosen to allow a 5.75x magnification of the MEMS array in an afocal imaging configuration. Of course, the field was compacted on its way towards the MEMS, and re-expanded after reflection, to its original size. After reflection from the MEMS and passage back through LP_M, the beam path was identical to that already covered for the plane mirror reflection. By placing the MEMS array in the back focal plane of the lens pair LP_M, the PSF measured by the CCD at the right end of the bench was for the field just after reflection from the MEMS. For the demonstration, the Hartmann WFS was not used to measure the MEMS reflections.

For this demonstration, the MEMS package was bonded and wired to a standardized mount that had a pin array on the underside. Figure 21 shows a photograph of the MEMS package as it appeared in the mount, after wire bonding. The mirror array has been highlighted by the white-dashed box. The MEMS package, as received from the foundry, is contained within the black-dashed box. Wires were connected between gold plated contacts on the mount and the bond pads visible along the four edges of the MEMS package. An experimenter's circuit box was configured with a zero-insertion force (ZIF)
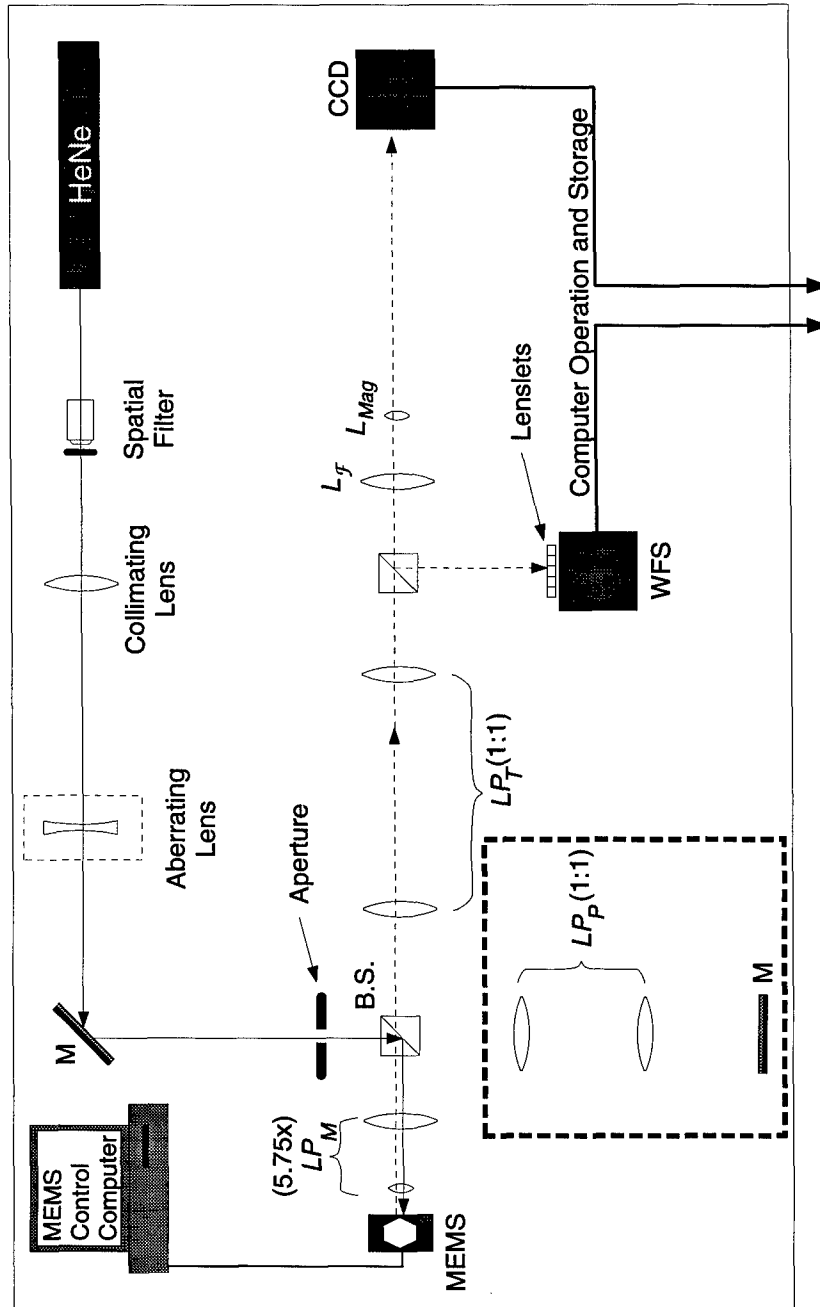
54

Figure 20.   The beam path for MEMS reflection measurements. The only measurement required for the demonstration is the PSF, recorded on the CCD to the right of the figure. Although the reflected field is shown reaching the WFS, no actual measurements were recorded for the demonstration.
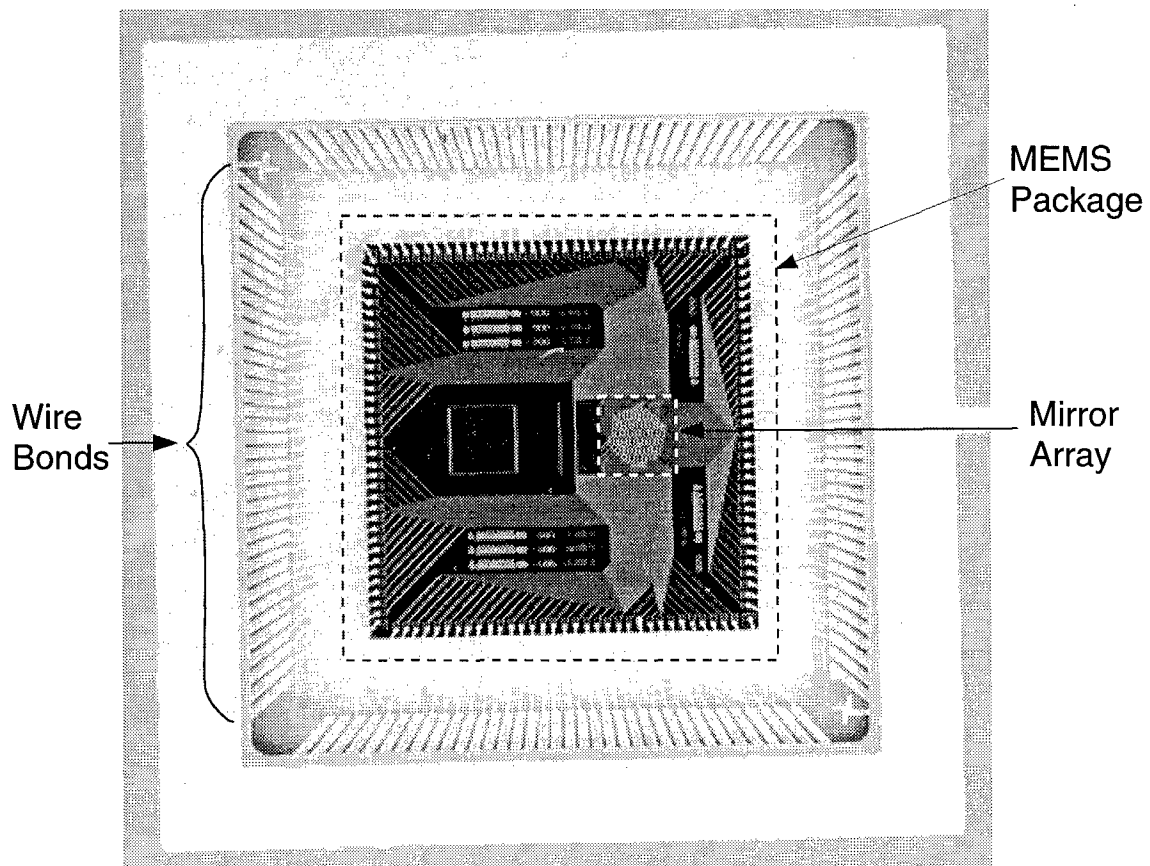
Figure 21.   Photograph of the entire MEMS package after wire bonding into the mount. The large, black-dashed box delineates the extent of the MEMS package as received from the foundry. The white-dashed box highlights the mirror array. The wire bonds were made between a gold plated contact on the mount and the bond pads manufactured around the edges of the MEMS package.

socket to hold the mounted package. Ribbon-cable connectors were also mounted on the box, and the pin connectors were wired to the contacts on the ZIF socket. The whole box was mounted on the bench for alignment of the MEMS with the optics.

A Greenspring Model ATC40 digital-to-analog (D/A) converter with 64 channels was used in an IBM compatible computer to provide the voltages to drive the MEMS mirrors. The voltage range used on the D/A converter was zero to 10 volts. The ribbon-cables from the MEMS circuit box were attached to the D/A channel connectors. We designed and wrote a software routine to interface with the D/A converter and allow easy configuration of the voltages required for the output channels. Since the D/A converter could only supply 64 separate voltages, not all the mirrors in the MEMS array were utilized for the demonstration. A scanning electron microscope (SEM) image of the whole MEMS mirror array is shown in Figure 22. Limited by 64 available channels in the D/A converter, we chose to operate 61 mirrors in the array. Figure 23 shows if the mirrors are numbered in rings, 61 mirrors completes a ring. Mirror #1 started in the center. For any given ring, the starting position was directly below the previous ring's starting position. Then, numbering proceeded clockwise around the ring. The channels in the D/A converter were wired to the mirrors so that channel one corresponded to mirror #1, channel two to mirror #2, and so on.

3.3.1 MEMS Characterization. A closer view in Figure 24 shows more detail of the flexure arms and topology of the micro-mirrors. The reflective surfaces of the MEMS were coated with a layer of gold, which doesn't have a remarkably high reflectivity at HeNe wavelengths, but it was the only reflective coating available at the manufacturing foundry. Although the mirrors were intended to be planar, subsequent measurements with a Zygo interferometer [33] indicated each mirror in the array was parabolic, tending to focus reflected light. The curvature resulted from a difference in the stress characteristics of gold and the poly-silicon substrate to which it was bonded.

A summary of selected device characteristics and dimensions is contained in Table 3. The first six entries in the table are self-explanatory. The next three entries describe the flexure arm and mirror sag, according to the geometry indicated by Figure 25(a).
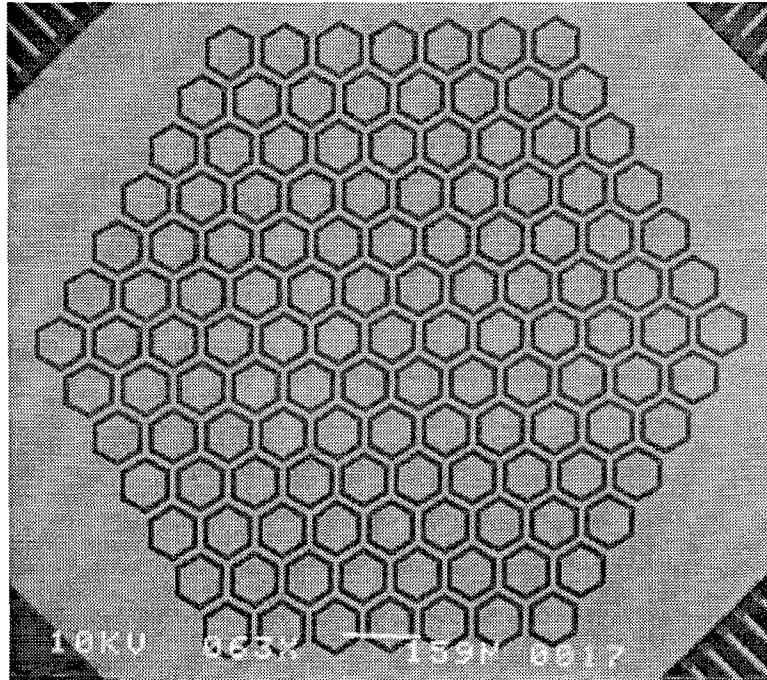
57

Figure 22.   SEM image showing entire MEMS mirror array. Some MEMS wire paths are visible in the corners of the image.
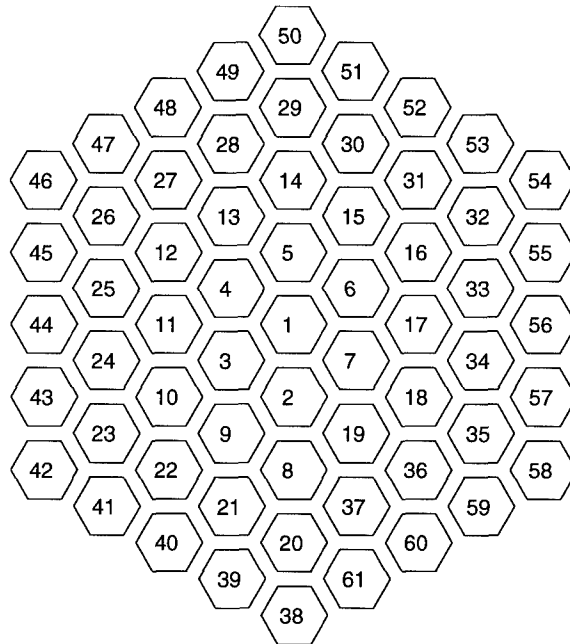

Figure 23.   Diagram indicating the numbering scheme used to relate a D/A channel to a mirror position.
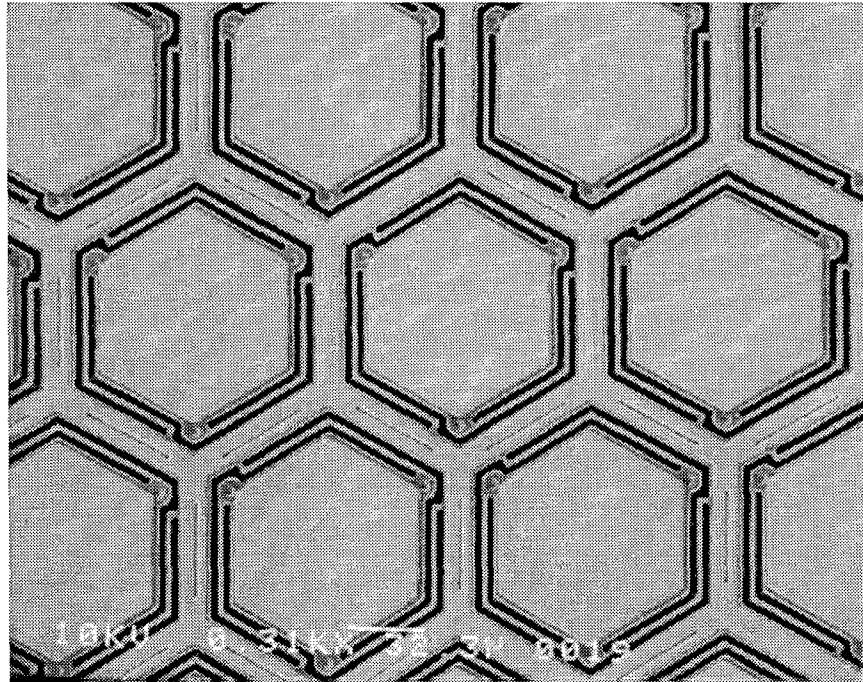
Figure 24. SEM image showing flexure arm detail and general topology of the MEMS mirror array.

MEMS Micromirrors	
Mirror Shape	Hexagonal
Mirror Dimension	46.9 μm on a side
Mirror Layout	Hexagonal
Center to center spacing	117 μm
Active Area	48 percent
Total Number of Mirrors	127
z_0	2.76 μm
d_{RMS} (average sag)	100 nm
z_{RMS}	2.66 μm
$\hat{k}$ (calculated in discussion)	1.198 x 10^{10} V/m$^{3/2}$

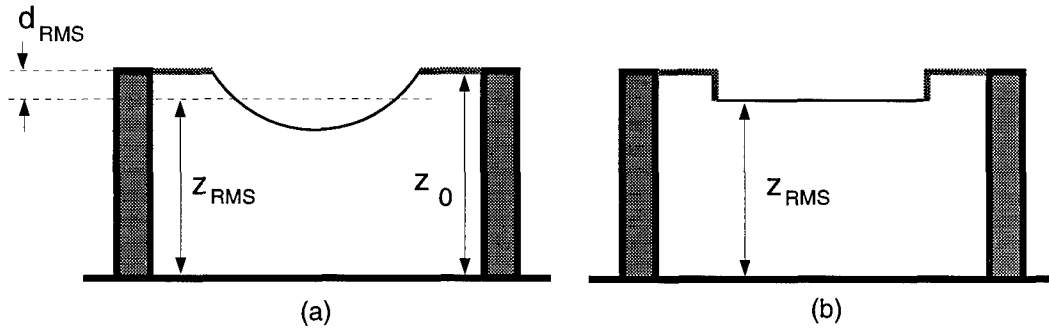Table 3. Selected MEMS micro-mirror array characteristics.

Figure 25.   Diagram (a) shows the parameters used to characterize the sag in a mirror element. Diagram (b) shows the plane mirror model used to calculate the voltages required for a desired deflection.

The flexure arm resting distance, z_0, was established by the design of the mirrors. The average mirror sag below the flexure arms, d_{RMS}, was measured directly with the Zygo interferometer. z_{RMS} was then calculated directly from these two quantities as the average distance between the mirror element and its underlying address electrode.

The final entry in Table 3 is the calibration constant of the mirror response to applied voltage, $\hat{k}$. The method used to calibrate the mirrors was to measure a known voltage and deflection pair, then calculate $\hat{k}$ using Equation 67. However, the method was complicated by two factors: the mirror surfaces were not planar, as assumed in deriving Equation 67, and it proved difficult to measure a deflection in an individual mirror for an applied voltage.

To proceed, let us first examine the consequences of the non-planar geometry of the mirror surface. This curvature must be accounted for in the control law of Equation 67, which was derived assuming planar mirrors. The voltage required to achieve a desired deflection is given by Equation 67, which is repeated here,

$$V = \hat{k}\left(z_0 - d_f\right)\sqrt{d_f}. \tag{68}$$

The geometry for the parameters is indicated in Figure 17. The design was for $z_0 = 2.76$ μm, and this is still the correct distance between the flexure arms resting position and the electrode, but with the mirror sag, a different value must be used in Equation 68. Using the parameter definitions indicated by Figure 25(a), we define $z_{RMS} = z_0 - d_{RMS}$, where
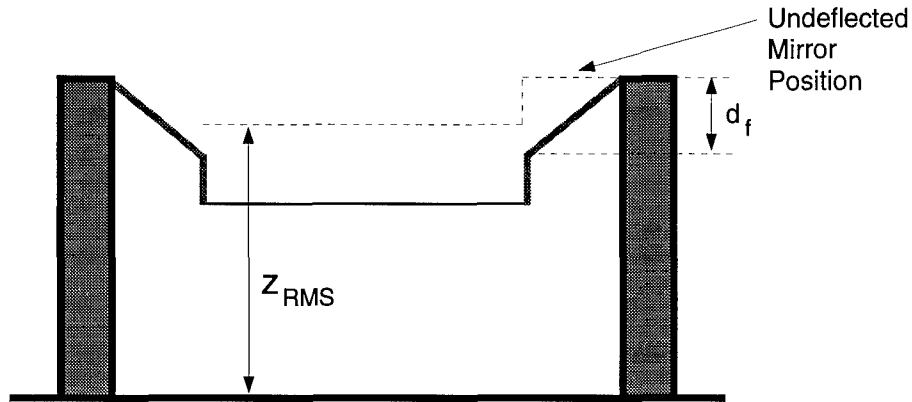
60

Figure 26. The geometry used to define the parameters used in the mirror deflection law.

d_{RMS} is the root-mean-square (RMS) sag in the mirror. Then, we modeled the mirror as planar, as indicated by Figure 25(b), but resting a fixed distance below the flexure arms. Then, substituting z_{RMS} for z_0 in Equation 68,

$$V = \hat{k} \left(z_{RMS} - d_f \right) \sqrt{d_f},\qquad(69)$$

becomes the relation to use to calculate a voltage for a desired deflection in the flexure arms. Figure 26 shows explicitly the situation for a deflection, d_f. The justification for Equation 69 is that the average electric field established between the curved mirror and the address electrode can be modeled as acting on a plane mirror lying z_{RMS} away from the address electrode. However, the flexure arms still rest at the same position, and it is the deflection from their resting position that provides the restoring force in the model.

Using a Zygo interferometer, the sag from flexure-arm attachment to the center of the mirror was measured as approximately 400 nm, and the RMS sag was $d_{RMS} = 100$ nm. Thus, $z_{RMS} = 2.66$ μm.

To perform a calculation of $\hat{k}$, a voltage and deflection pair must be measured. It has been demonstrated that the mirrors become unstable in deflection when the mirror moves past a third of the way towards the electrode [9]. Beyond this critical deflection distance, the mirrors tend to suddenly "slam down" into the electrode. It has been observed by us, that when a MEMS device is placed in the Zygo interferometer, it is easy to tell

61

when a mirror slams down all the way to the substrate. The voltage required to slam the mirror corresponds to a deflection $d_f = z_{RMS}/3$. Thus, to determine $\hat{k}$, the MEMS were placed under a Zygo interferometer and a voltage supply was wired to a non-critical mirror in the field of view. The voltage was adjusted in increments until the mirror slammed down. The noted voltage was 20 volts, and from this observation, a benchmark value of $\hat{k} = 1.198$ x 10^{10} V/m$^{3/2}$ was determined using Equation 68.

This benchmark value was used as the calibration for all the mirrors in the array, as it was not feasible to measure a response for each mirror. Slamming the mirrors down is a potentially destructive test, as this causes a short circuit between the mirror substrate and the electrode. The small area of the devices results in a large current density, which rapidly raises the temperature of the contact to the point that the mirror substrate fuses to the electrode. One protection measure is to include a resistor in series with the voltage applied to a mirror, to act as a current limiter in the event of slamming a mirror. From observations using the Zygo interferometer, the vast majority of slammed mirrors protected with a series resistor were able to recover. Since MEMS devices were a scarce resource, we decided to be conservative on the side of preserving devices rather than attempting to perform a complete characterization.

In addition, the utility of a complete characterization is questionable. In his device characterizations, Michalicek did not report experiencing large deviations in mirror response among mirrors on the same device [9]. However, Christensen did experience large deviations in mirror response for his beam steering demonstration [16]. Also, it has been observed that the MEMS device characteristics change over time as the poly-silicon absorbs water from the natural humidity in the air. Dust particles attracted to the charged surfaces may become lodged under a mirror, affecting its ability to deflect. The combined result is that each MEMS device has a limited practical lifetime unless precautions are taken to protect it from humidity and dust, especially while in operation. No such precautions were taken for this demonstration. It should be noted that Michalicek's characterizations were conducted in a vacuum chamber, while Christensen attempted to protect his device in a nitrogen rich environment (it wasn't sealed, just over pressurized).
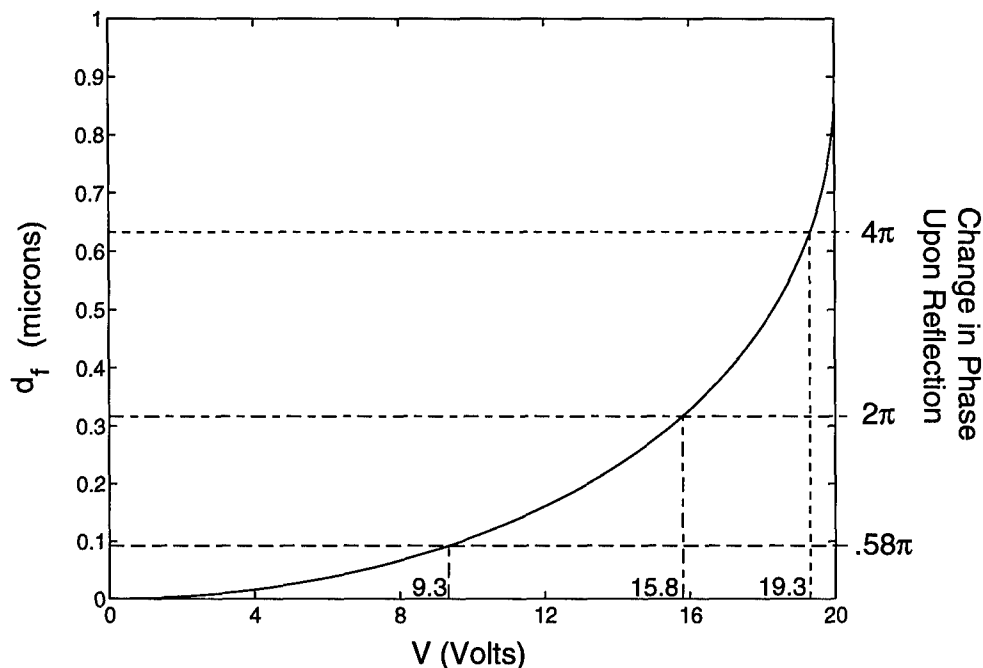
Figure 27. Calculated mirror deflection vs. voltage for the devices used in the demonstration. The right vertical axis shows selected changes in phase that would result for a HeNe wavelength wave front reflection ($\lambda = 632.8$ nm): the corresponding voltage is indicated on the horizontal axis. The dashed lines indicate the range of operation for the MEMS device using a 0 to 10 Volt D/A converter and an external DC bias.

We attempted to use the Zygo interferometer to characterize a mirror deflection in a non-destructive manner, but our attempt was frustrated by the discontinuous nature of the MEMS reflections. No continuous fringe lines exist between mirror and supporting post. Thus, the microscope cannot count fringes from a constant reference point, and no relative deflection measurement was possible. A demonstration performed by Lin used an interferometric microscope in a different manner than we attempted [26]. His technique would allow a non-destructive characterization to take place, but our discovery of his technique occurred too late in the research effort to be of use.

3.3.2   Biasing the MEMS.   Using the value of $\hat{k}$ computed for Table 3, the deflection vs. voltage curve shown in Figure 27 was calculated by Equation 69. The right,
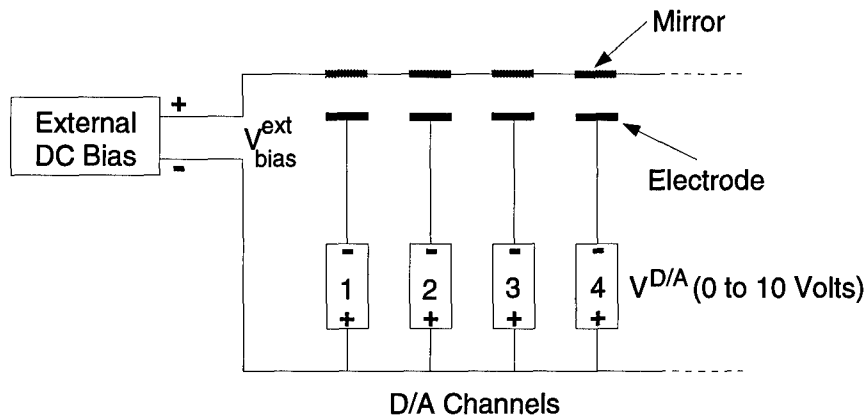
63

Figure 28. Diagram showing the bias and D/A channels circuit. The MEMS device provided contacts to bias all the mirrors to a common voltage. The D/A converter was referenced to a floating ground, allowing each channel to change voltage relative to the external bias.

vertical axis indicates selected values of the change in phase that would result from a HeNe wavelength wave front reflection. For a given deflection, d_f, the resulting change in phase upon reflection is related by $\Delta\phi = (4\pi d_f)/\lambda$. In operating the MEMS as a deformable mirror, the mirrors could only deflect towards the substrate. To correct a general, piston-removed aberration, both positive and negative changes in phase were required of the MEMS. To handle this situation, the mirrors were first biased to the 2π reflection point $(d_f = \lambda/2)$, thus making the MEMS appear undeflected to the wave front. The mirrors were then adjusted above and below the 2π point to compensate for the piston removed aberration.

The MEMS device provided contacts that were used to charge the mirrors to a common bias voltage relative to the electrodes. Then, the D/A channel was used to provide a voltage to an individual electrode, relative to the bias, that would result in the desired potential difference. The equivalent circuit diagram is shown in Figure 28.

From Figure 27, we see that the 2π reflection point corresponded to a voltage of 15.8 Volts. This was the overall, required bias voltage for the mirrors, but since the D/A converter used in the demonstration was only capable of operation in the range of zero to 10 Volts, an external bias had to be used in combination with a D/A supplied bias to reach the total, required 15.8 Volts. Examining the circuit diagram of Figure 28 shows

64

that the use of a fixed, external bias meant a zero voltage could not be applied to the mirrors. With the range of motion limited by the external bias, it was selected to be as small as possible, thereby allowing the largest range of motion for the mirrors about their 2π deflection point. Thus, we wanted to select a D/A bias voltage as large as possible, to minimize that required of the external supply.

Ideally, we would like to be able to operate $\pm 2\pi$ around the bias position. Reaching a 4π phase change was not a problem, as indicated by Figure 27. Assigning,

$$V_{2\pi} = 15.8 \text{ Volts}, \tag{70}$$

$$V_{4\pi} = 19.3 \text{ Volts}, \tag{71}$$

as the voltages required for a 2π and 4π change in phase, we see that we needed the D/A converter to supply,

$$\Delta V = V_{4\pi} - V_{2\pi} = 3.5 \text{ Volts} \tag{72}$$

above the 15.8 Volt total bias to reach $V_{4\pi}$. By selecting the D/A bias voltage to be 3.5 Volts below its maximum possible value, it supplied as much bias voltage as possible, thereby minimizing the external bias voltage required to reach 15.8 Volts. With the maximum D/A voltage as $V_{max}^{D/A} = 10$ Volts, we see that the D/A bias voltage should be,

$$V_{bias}^{D/A} = V_{max}^{D/A} - \Delta V = 6.5 \text{ Volts}. \tag{73}$$

This meant that the external bias needed to supply,

$$V_{bias}^{ext} = V_{2\pi} - V_{bias}^{D/A} = 9.3 \text{ Volts}, \tag{74}$$

to reach a total bias voltage of 15.8 Volts for the combination of D/A converter and external bias supply. This combination gave the maximum range of motion for the MEMS, where $V_{bias}^{D/A}$ now represents a starting voltage for all D/A channels. By adjusting the channel voltage above or below $V_{bias}^{D/A}$, a positive or negative change about the 2π position can be achieved. With the external supply fixed at V_{bias}^{ext}, the minimum possible voltage that could

be applied to the mirrors was 9.3 Volts. This voltage value is shown in Figure 27, and the corresponding minimum change in phase is seen to be 0.58π radians.

3.3.3 Selection of the Aberrating Focal Length. The required bias voltage limited the range of aberrations we could correct, which necessitated careful selection of the aberrating focal length, f_a, used in the setup so as not to exceed the limits we could correct. With the MEMS magnified by a factor of 5.75x, they appeared on the Hartmann CCD as shown in Figure 29. As indicated by the superimposed numbering, all the mirrors in the field of view corresponded to a D/A channel. Thus, as long as the piston removed aberration didn't exceed $\pm1.42\pi$ across the Hartmann CCD, the mirrors could be adjusted to fit the phase profile.

From the previous discussion, the field just past the adjustable aperture in Figure 18 is the field that is eventually measured on the Hartmann WFS and CCD recording the PSF. Let R represent the radius of curvature of a spherically aberrated field when it reaches the adjustable aperture. The geometry of the field as it reaches the aperture is shown in Figure 30. x represents the radius of the adjustable aperture, and the dashed curve represents the curvature of the field when it reaches the aperture. s is twice the maximum distance the MEMS can deflect about the 2π point (a given deflection corresponds to twice the resulting change in the reflected phase). It is obvious from the geometry that,

$$R^2 = x^2 + (R - s)^2. \tag{75}$$

Expanding and solving for R as a function of s and x yields,

$$R = \frac{s^2 + x^2}{2s}. \tag{76}$$

For a plane wave incident on a lens of focal length f, the resulting transmitted wave will be spherical with radius $R = f$ [30:100]. Thus, since we desire a slightly expanding spherical wave, we should use Equation 76 to choose a minimum focal length f_{min} from,

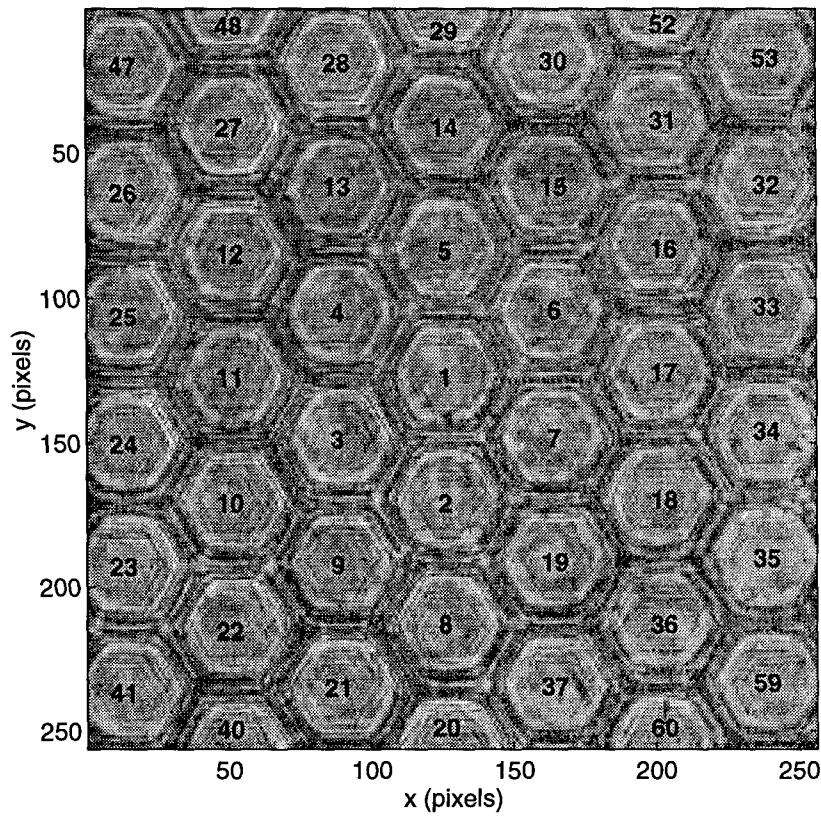$$f_{min} = -\frac{s_{max}^2 + x^2}{2s_{max}}, \tag{77}$$

66

Figure 29. CCD image of the MEMS mirrors as they fill the Hartmann aperture. The geometry was chosen so the aperture was filled with active mirrors.
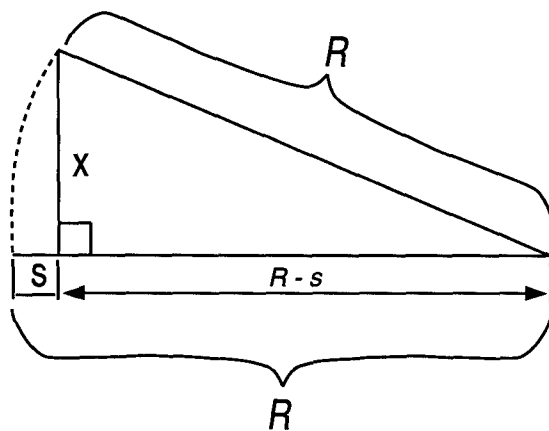

Figure 30. Geometry of maximum spherical aberration, R, at adjustable aperture, width x.

for a given x and s_{max}. From our setup, we see that $x = 2$ mm (half the width of the Hartmann CCD), and $s_{max} \approx .45$ μm (the maximum change in optical path length we can absolutely correct). Then,

$$f_{min} \approx -4.4 \text{ m.} \tag{78}$$

Our selection of $f_a = -3.5$ m is justified, since the aberrating lens is greater than 1 meter away from the adjustable aperture. Thus, as long as the aberration is reasonably centered with the rest of the optics train, including the MEMS, we will be able to fit the MEMS to the aberration without difficulty.

This concludes the discussion of the experimental setup and components used for the demonstration. The next section covers the various procedures used to collect and process the data.

3.4 Procedures

3.4.1 Overview.
The steps in the demonstration are outlined below, with a few words about the measurements and calculations required at each step. Then, each step is discussed more thoroughly in the following subsections. Unless otherwise mentioned, all software routines were implemented in **MatLab©**.

- **CCD Calibration**
  Data was collected to be used in calibrating the images stored from each CCD. In particular, a set of dark field and flat field frames were stored for each CCD before actual data was taken.

- **Measurements with No Aberration**
  First, the MEMS path was covered and sets of PSF and Hartmann WFS CCD images were stored. Then, the plane mirror was covered and a set of PSF images were stored for a MEMS reflection.

- **Measurements with an Uncorrected Aberration**
  The aberrating lens was added to the setup. The MEMS leg was covered and both PSF and Hartmann WFS CCD images were stored for the plane mirror reflections.

Then, the MEMS leg was uncovered and PSF images stored for both biased and unbiased MEMS configurations.

- **Wave Front Reconstruction**

  Using the Hartmann WFS CCD images for plane mirror reflections, the aberrated wave front phase was reconstructed by the methods of Section 2.5.

- **Calculate Required Voltages**

  Then, the voltage required for each MEMS mirror was calculated using Equation 69 and the bias information.

- **Measurements with a Corrected Aberration**

  The voltages were loaded into the D/A converter and applied to the MEMS mirrors. The resulting PSF images were stored from the CCD.

- **Analyze the Changes in the PSF**

  The final step was to examine the saved PSF images and identify changes that resulted from correcting the aberration. A radial average intensity routine was used on each image to compare PSF intensity distributions between images.

3.4.2 CCD Calibration. Two calibrations measurements were required for a CCD. The first was a "dark frame", where the lens cap was placed over the CCD and images were stored that indicated the noise from the dark current for each pixel in the array. The other measurement was a "flat field", which is an indicator of the difference in response for each pixel to a given intensity of light. A white light source illuminated a white screen in front of the CCD, and the resulting image was stored. The illumination was chosen to put the pixels near their maximum intensity, so that noise effects were minimal on the resulting image.

For each calibration, multiple frames were stored to disk. Then, the frames were averaged to produce an average response for each calibration. To illustrate the use of the recorded calibrations, consider a subsequent measurement where an uncorrected CCD image is stored. Let the pixels in the uncorrected image be represented by $p_u(i,j)$ where i,j are the row and column indices for the CCD array. The pixels in the previously recorded average dark frame are represented by $p_d(i,j)$ and the flat field is represented by $p_f(i,j)$.

First, the flat field is normalized, such that,

$$p_f(i,j)_{norm} = \frac{1}{\max(p_f)} p_f(i,j). \tag{79}$$

Then, the corrected image pixels, $p_c(i,j)$, are calculated from,

$$p_c(i,j) = \frac{p_u(i,j) - p_d(i,j)}{p_f(i,j)_{norm}}, \tag{80}$$

where the equivalent dark current intensity has been subtracted and the resulting pixel intensity normalized to the flat field response.

The dark frame and flat field response of the CCD tend to change over time as the camera heats up. By letting the camera warm up for an hour before using it, the calibrations were stable during the data collection.

3.4.3 Measurements with No Aberration.

The initial measurements were performed without the aberrating lens in the setup. Before using the Hartmann WFS, the lenslets had to be aligned with the CCD to produce an acceptable image. By observing the real time Hartmann image on the computer monitor, the lenslets were adjusted until they provided a centered, level array of intensities on the CCD. It was recognized that perfect alignment was not critical: any misalignment would be subtracted from subsequent data through the use of a reference measurement.

With the MEMS reflection leg covered, a reference WFS measurement was recorded for a plane wave reflection off the plane mirror. Multiple Hartmann CCD images were stored to disk for later averaging. Then, the plane wave PSF was recorded with the other CCD.

The plane mirror was then covered, and the MEMS were exposed to the planar wave front. The resulting PSF was recorded on disk.

3.4.4 Measurements with an Uncorrected Aberration.

With the unaberrated measurements complete, the aberrating lens was added to the setup. The MEMS were covered and measurements were taken of the plane mirror reflection with both the Hartmann WFS

and the CCD recording the PSF. We desired the aberration to be as centered as possible with the MEMS and the Hartmann, so we performed reconstructions to examine the relation of the aberration to the Hartmann CCD. The next section covers the details of a wave front reconstruction. It took many adjustments and repeated measurements to get the aberration centered. The final form of the aberration will be presented in the next chapter.

Once the aberration was centered, the plane mirror was covered and the MEMS were exposed. With no voltage bias, the PSF was recorded for the uncorrected aberration. Then, the MEMS were biased to their 2π reflection point and the resulting PSF was recorded for comparison.

3.4.5 Wave Front Reconstruction. At this point, we needed to reconstruct the aberration, so we could calculate the displacements required for each mirror in the MEMS array. This section uses the theoretical developments of Section 2.5.

Only the two Hartmann WFS measurements are of interest to the wave front reconstruction: the unaberrated plane mirror reflection, and the aberrated plane mirror reflection. The unaberrated data was used to generate reference slopes to subtract from the raw slopes computed for the aberrated wave front. The first step in the process was to average the multiple Hartmann CCD frames for each measurement and produce two average frames. This was performed in a separate routine before the processing software was used to calculate the slopes.

The general algorithm used to calculate the slopes from a raw CCD frame (whether averaged or not) is outlined in Figure 31. First, the reference slopes from the unaberrated plane wave were calculated and saved using the algorithm. Then, the slopes from the aberrated CCD image were calculated using the previously stored reference slopes.

With the slopes in hand, the reconstruction of the wave front was performed using a set of triangle basis functions. The triangle function is defined as,

$$\text{tri}(x) = \begin{cases} 1 - \left| \dfrac{x - x_c}{b} \right|, & \left| \dfrac{x - x_c}{b} \right| < 1 \\ 0, & \text{elsewhere} \end{cases} , \tag{81}$$

71

Algorithm For Slope Calculations from Hartmann CCD Data
Load Flat Field
Load Dark Frame
Load Data Frame
Calibrate the Data Frame
For each Hartmann subaperture
     Put the 13 x 13 array of pixels for the subaperture into a SubFrame
     Calculate the SubFrame center of x-intensity, x_{cen}
     Calculate the SubFrame center of y-intensity, y_{cen}
     Calculate the slopes from $s_q = f q_{cen}(2\pi)/\lambda$
     Next subaperture
Load Reference Slopes (optional)
Subtract Reference Slopes, if provided
Store resulting slopes for later use

Figure 31. General algorithm for calculating wave front slopes.

where the function is centered at x_c and its extent is limited to $\pm b$ on either side of its center location. For the reconstructions, a regularly spaced, 15 x 15 array of tri functions were chosen to populate the Hartmann aperture. The tri function centers were evenly distributed throughout the aperture, separated by .29 mm. By selecting $b = .29$ mm, each tri function overlapped with its neighbors.

Following the methods of Section 2.5, a reconstruction matrix **M** was calculated by Equation 57 for the triangle basis functions. A separate Fortran routine calculated and saved **M** to disk for later use. Using the slopes calculated for the aberrated wave front, Equation 44 was used to calculate the appropriate weights, **c**, for use in reconstructing $\tilde{\phi}(\vec{x})$ from Equation 41.

The resulting **c** was stored to disk. A software routine was written which allowed computation of the piston removed phase value for any point in the aperture. The routine loaded **c** as needed and returned the requested phase to the calling routine. Built in MatLab© plotting routines were used to view the resulting wave front reconstruction in three dimensions.

3.4.6 Calculate Required Voltages. The center position of each mirror in the Hartmann aperture was known from the hexagonal geometry of the mirrors and confir-

mation of their orientation as shown by Figure 29. The algorithm used to fit the MEMS to the wave front was simple: match each center position of the MEMS to the wave front piston removed phase as contained in the reconstruction.

Thus, a function call was made to a software routine to provide the phase for each mirror center location. Using this value of the phase, the relative mirror deflection about the bias position was calculated, then translated into an absolute deflection. The voltage required to achieve the absolute deflection was computed from Equation 69, then adjusted for the external bias voltage. The resulting voltage was the value to be provided by the D/A converter.

3.4.7 Measurements with a Corrected Aberration. The required voltages were saved to file in an ASCII format, one voltage per mirror. The file was transferred to the MEMS control computer, and a C code software routine read the file and set the D/A converter channels to the correct voltage. With the mirrors in the correct position, the corrected wave front PSF was recorded by the CCD.

3.4.8 Analyze the Changes in the PSF. The recorded PSF images were transferred to a Sun workstation for further analysis. **MatLab©** routines were written that allowed easy viewing and manipulation of the pixel arrays stored by the CCD. An additional software routine allowed the radial average intensity of each PSF to be calculated as a function of distance from the center of the pattern. This allowed direct comparisons to be made between different PSF images, and the effects of the MEMS correction were made apparent. The next chapter discusses the details of the results.

IV. Analysis and Results

4.1 Overview

This chapter starts by presenting the results of the plane mirror reflections for aberrated and unaberrated wave fronts. These results showed that the setup was working as expected, and they provided the reconstructed, aberrated wave front phase for use in configuring the MEMS for later results. The effects of MEMS reflections on aberrated and unaberrated plane waves are then presented. Finally, the corrected aberration results are compared to the uncorrected aberration reflections.

4.2 Plane Mirror Reflections

An unaberrated plane wave was used to generate a reference wave front measurement for use with subsequent Hartmann WFS reconstructions. Figure 32 shows the three dimensional reconstruction of this reference measurement. This reconstruction shows the fixed optical aberrations present in the optics. The dominant feature is clearly the large degree of tilt, although we suspect that the tilt is artificial: for WFS measurements, it is difficult to align the lenslets with the center of the CCD used for the Hartmann WFS. A misalignment will shift all the intensity patterns in a common direction, inducing a constant degree of slope in every subaperture measurement. But, the reference is seen to be predominantly planar, as expected.

The reconstruction in Figure 33 shows the aberrated wave front after adding the long, negative focal length lens to the system. The reconstruction was performed by subtracting the reference slopes taken for Figure 32 from the slopes measured after the aberrating lens was introduced. Thus, the reconstructed phase in Figure 33 is due only to the changes to the wave front from the aberrating lens. The aberration is seen to be symmetric, if not exactly centered, and is the form we would expect for an expanding spherical wave.

As established in Chapter 2, the far field diffraction pattern of the system is equivalent to the point spread function. The resulting point spread functions for the plane wave and aberrated wave front are shown in the CCD images of Figures 34 and 35. All the CCD images in this section are negative images where dark areas signify high intensity, and
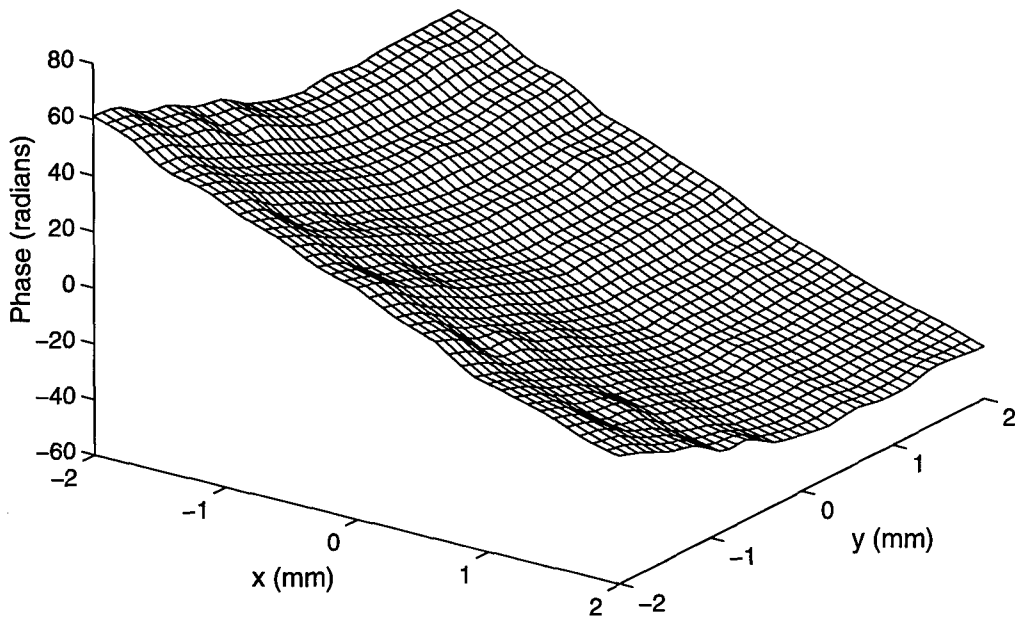
74

Figure 32.   Wave front reconstruction of an unaberrated plane wave reflection off a plane
mirror. Tilt is the dominant aberration, mostly from a non-normal incidence
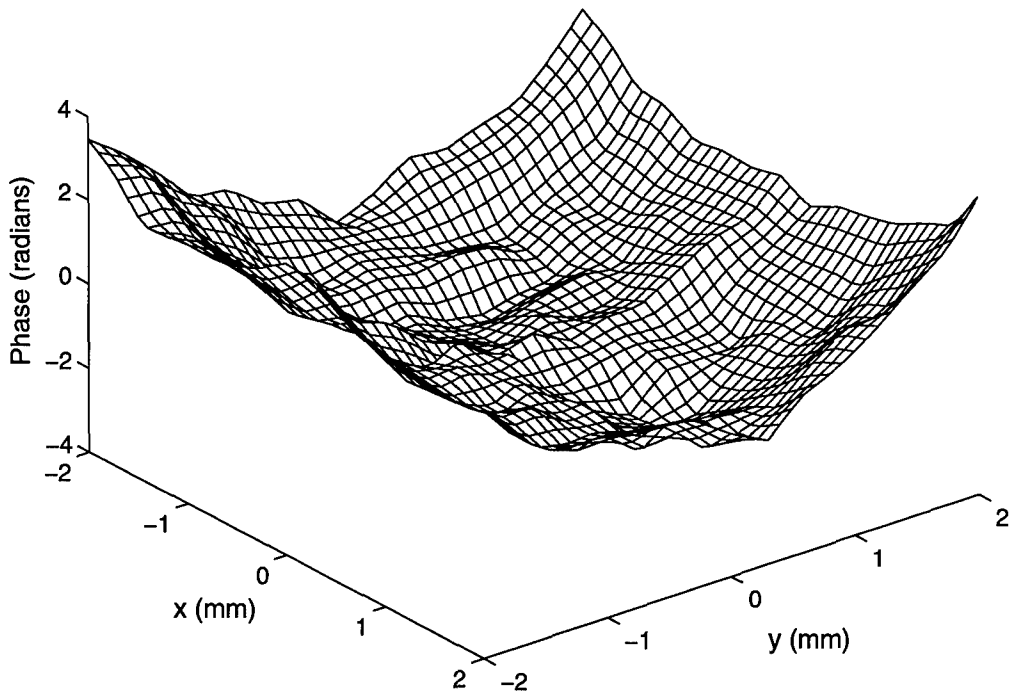of the wave front with the WFS.

Figure 33.   Wave front reconstruction of the aberration induced on the planar wave front by a negative focal length lens.
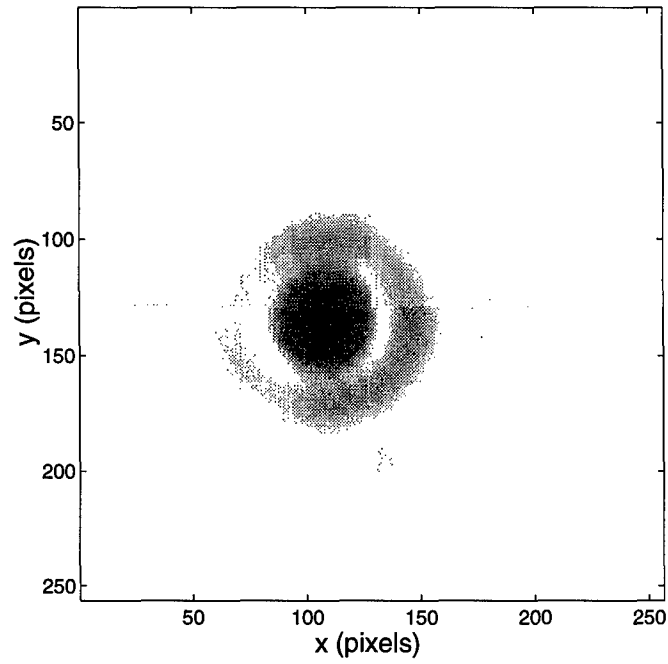
Figure 34.   PSF for a plane wave reflection off the plane mirror. Like all CCD images in this section, this is a log amplified, negative image.
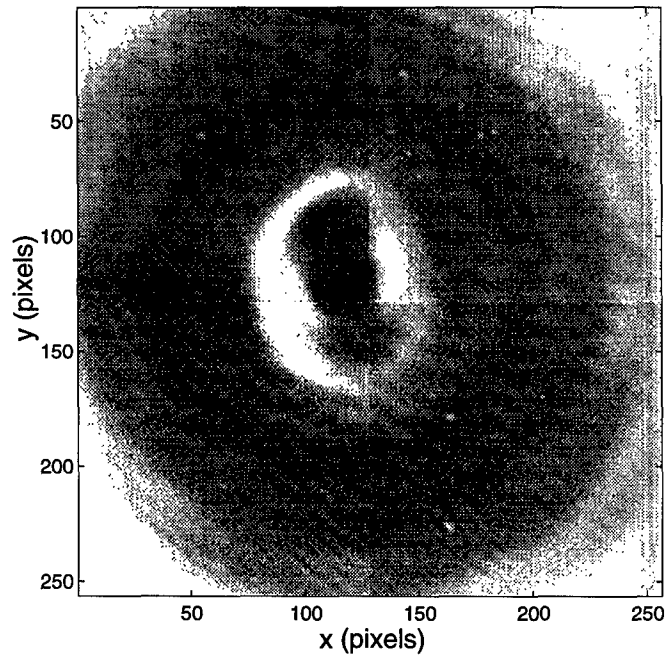

Figure 35. PSF for the spherically aberrated plane wave reflection off the plane mirror.
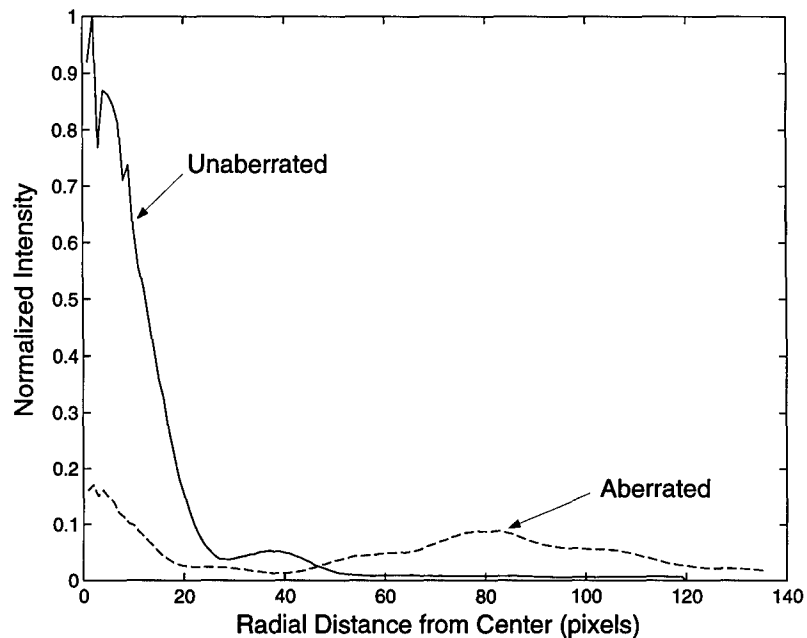
77

Figure 36. Comparison of the radial average PSF intensities for an aberrated and un-aberrated plane wave.

white areas are low intensity. In addition, all the CCD images are "log amplified" to bring out dim features not apparent in a non-amplified image. The natural logarithm is taken of each pixel intensity in the image, then the result is normalized to a 256 gray scale. The result is that each CCD image is normalized to its own peak value, so the images are not directly comparable with each other.

The unaberrated PSF in Figure 34 shows the typical Airy disk pattern expected for such an image. The aberrated PSF in Figure 35 shows clearly that the optical energy has been spread out, consistent with the expected far field diffraction pattern of a spherically aberrated beam.

To compare the figures more directly, consider the plots of radial average PSF intensity shown in Figure 36. The plot was generated from the non-amplified, raw intensity data used to generate Figures 34 and 35. The center of the distribution was identified for each PSF, then the average intensity as a function of radial distance from the center was

calculated. Each PSF intensity distribution was normalized to the maximum value for the unaberrated plane wave.

The result of the aberration on the radial average PSF intensity is to dramatically decrease the peak intensity and increase the relative intensity of the pixels beyond the central diffraction order. Note that in the unaberrated PSF (solid line), the extent of the central diffraction order is better defined: it drops convincingly towards zero before rising again on the first Airy ring. The aberrated PSF central order is seen to plateau around a radius of 20 pixels, before dropping to its first minimum at 40 pixels, where it again rises on the outer rings. This effect is apparent from Figure 35, where the central lobe is seen to wash out with the first ring at the top and bottom of its extent, and the outer rings are almost as intense as the central lobe.

This concludes the plane mirror reference measurements. We will return to an examination of these figures in comparing the results from the MEMS reflections.

4.3   Uncorrected MEMS Reflections

Now consider the effect of reflecting the wave front off the MEMS and measuring the PSF. We'll start by considering the overall diffraction pattern, then focus attention on the central order, which is of interest for this demonstration. Figure 37 shows the overall far field diffraction pattern for an unaberrated plane wave reflection. As before, the figure is a log amplified, negative image. The figure shows that the segmented, periodic structure of the MEMS has diffracted much of the reflected energy into higher orders. The hexagonal symmetry of the pattern is obvious, and it is due to the hexagonal shape of the reflective elements. Since we lose significant energy to higher orders, we expect the peak intensity in the central order to be lower than that for the plane mirror reflection shown earlier.

As evidenced by the results of the plane mirror reflections, we expect the most dramatic changes in the PSF to occur around the central order for an aberrated wave front. The changes in the higher diffraction orders shown in Figure 37 are too small to notice on this scale. Thus, the measurements taken for the demonstration will be of the PSF in the vicinity of the central diffraction order. For a real adaptive optics system, the
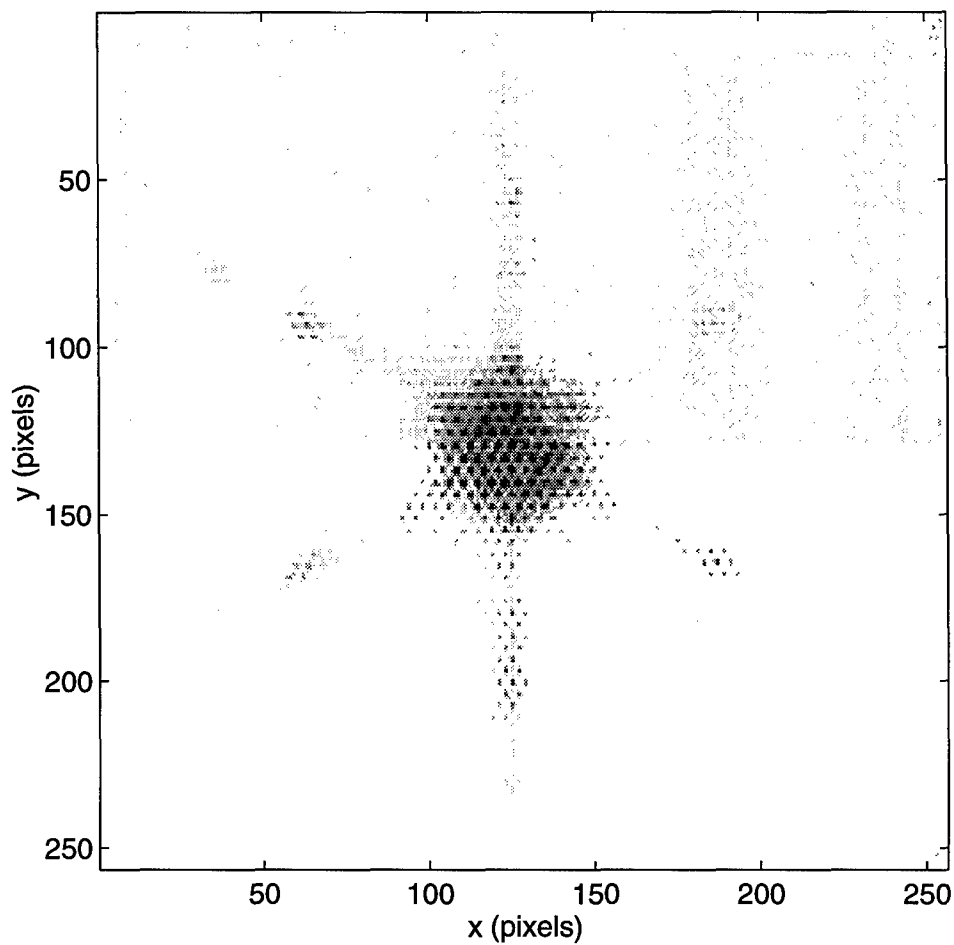
Figure 37. An image of the far field diffraction pattern for an unaberrated plane wave reflection off the MEMS, showing the higher diffraction orders of the reflection. The higher orders extend far away from the central order and exhibit the hexagonal symmetry imparted by the geometry of the reflective elements.

central order would be the order utilized by the system, and its response to wave front aberrations is of prime interest.

Figure 38 shows the PSF of just the region around the central MEMS diffraction order for an unaberrated, plane wave reflection. Just below it, Figure 39 shows the PSF for the aberrated wave front reflection off the MEMS. Both reflections were taken with non-deflected mirror elements. As before, the images are log amplified, negative images, normalized to their own peak values. Examining Figure 38, we see that the central PSF order has some structure to it, similar to the structure of the Airy disk pattern for the plane mirror reflection. In the aberrated case of Figure 39, the intensities of the off-center regions have increased relative to the central order, which is now dramatically smaller than the unaberrated central order above it.

A plot comparing radial average PSF intensities from the original intensity data used for Figures 38 and 39 is shown in Figure 40. The intensities are normalized to the peak value of the unaberrated reflection. As seen for the plane mirror case, the most dramatic difference is the relative decrease in peak intensity from the aberrated wave front. Additionally, the relative off-center intensities have increased. The unaberrated PSF (solid line) shows an Airy ring-like rise after falling to zero around pixel radius 30. The unaberrated curve shows that its intensity is concentrated close to the central order. The aberrated PSF has large relative intensities in regions away from the central peak, as expected from the results of the plane mirror reflections.

Comparing Figure 40 to Figure 36, the change in PSF between aberrated and unaberrated reflections is qualitatively the same. However, the effect of using the MEMS instead of the plane mirror for the reflection significantly reduces the absolute peak intensity of the central lobe. The peak of the unaberrated curve in Figure 40 is only 0.16 the value of the peak for the unaberrated curve in Figure 36. This shows that the MEMS tends to diffract a large amount of reflected energy into the non-central orders.

With knowledge of the aberrated phase from the plane mirror reflections, we are ready to calculate and apply the voltages required to match the aberration with the MEMS mirrors.
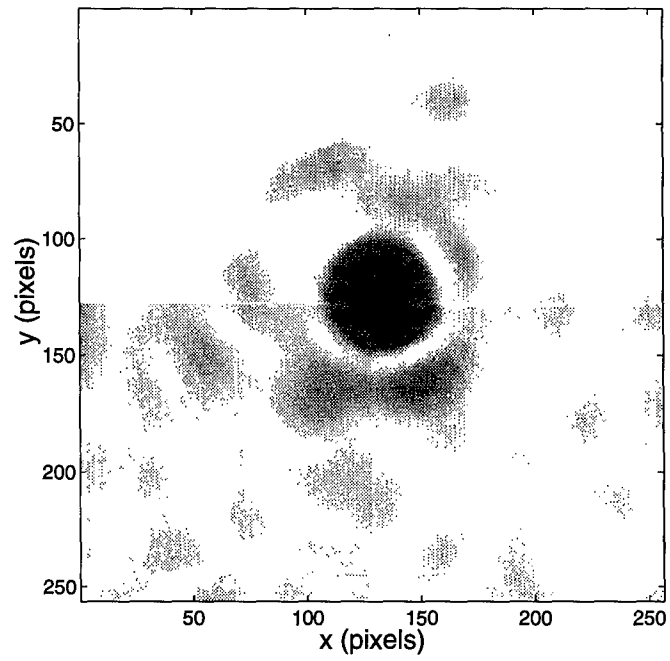
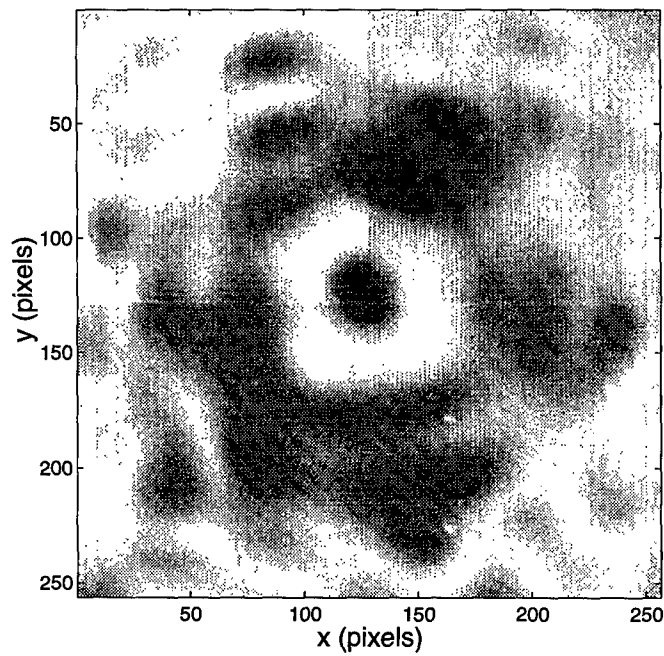Figure 38. PSF of the central order for a plane wave MEMS reflection.

Figure 39. PSF for a MEMS reflection of a spherically aberrated plane wave.
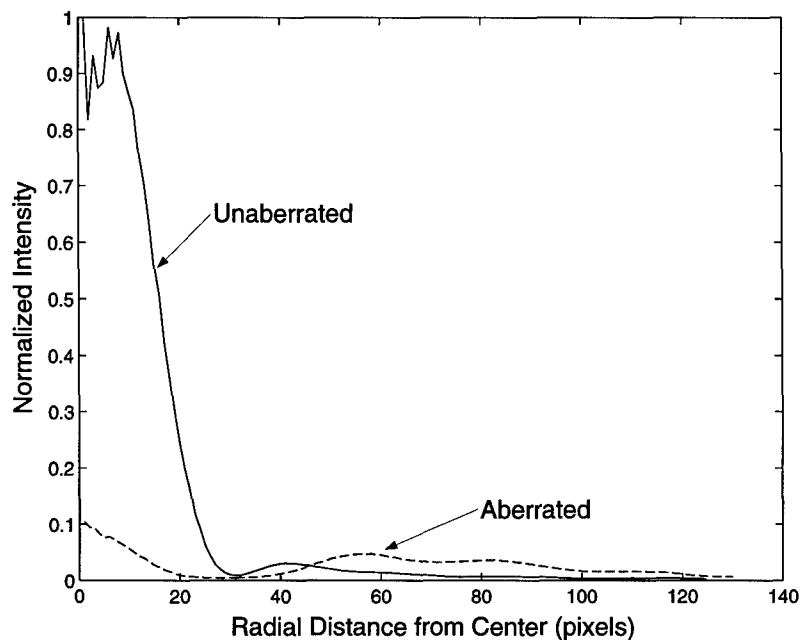
82

Figure 40. Radial average PSF intensity distribution for a MEMS reflection of an aberrated and unaberrated wave front.

4.4 Corrected MEMS Reflections

The first step is to deflect the MEMS mirrors to their bias position. With the external bias set to 9.3 Volts, and each D/A channel at 6.5 Volts, the mirrors will be deflected to their calculated 2π reflection point as indicated by Figure 27. The resulting PSF of the aberrated wave front reflection is shown in Figure 41. For comparison, Figure 42 shows the radial average intensity of Figure 41 with the radial average intensity of Figure 39 (the aberrated reflection off non-deflected mirrors). The effect of biasing the mirrors is seen to be most dramatic in the loss of resolution of the off-center peaks. Ideally, the two curves in Figure 42 would be nearly identical, since we are attempting to bias the mirrors to the 2π reflection point. Unfortunately, errors in calibration and response are inevitable, thus we don't quite make a perfect match. However, it is encouraging to note that the peak value has not changed dramatically, and the off-peak intensities are approximately the same magnitude.
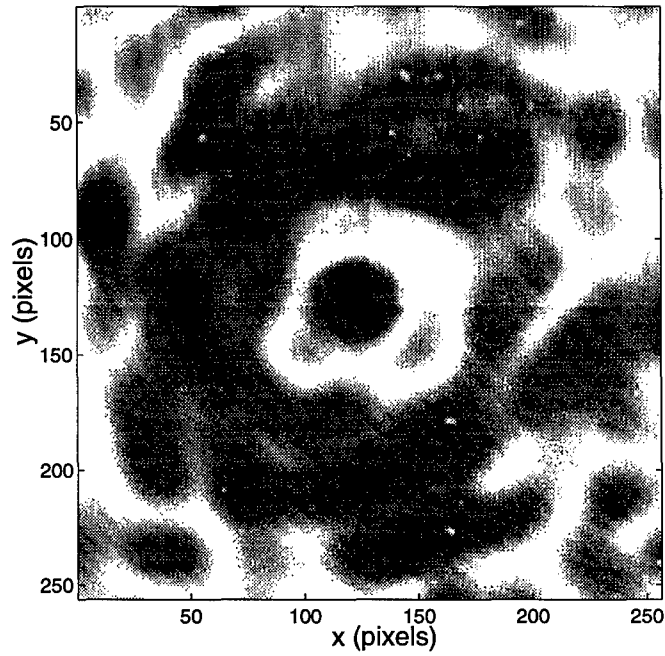
Figure 41.   PSF of the uncorrected, aberrated MEMS reflection with the mirrors in their
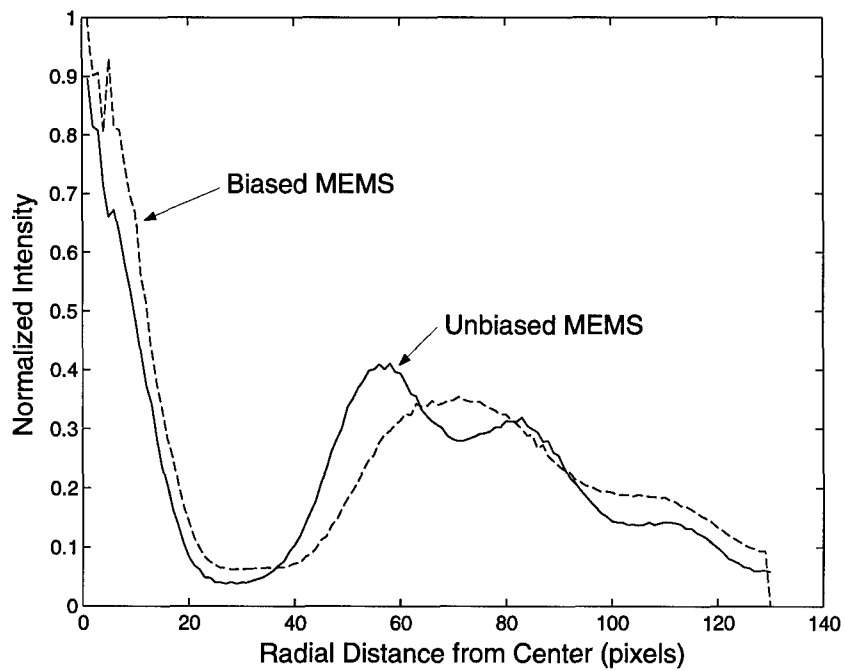bias position.

Figure 42.   Radial average PSF intensity comparison for an aberrated wave front reflection
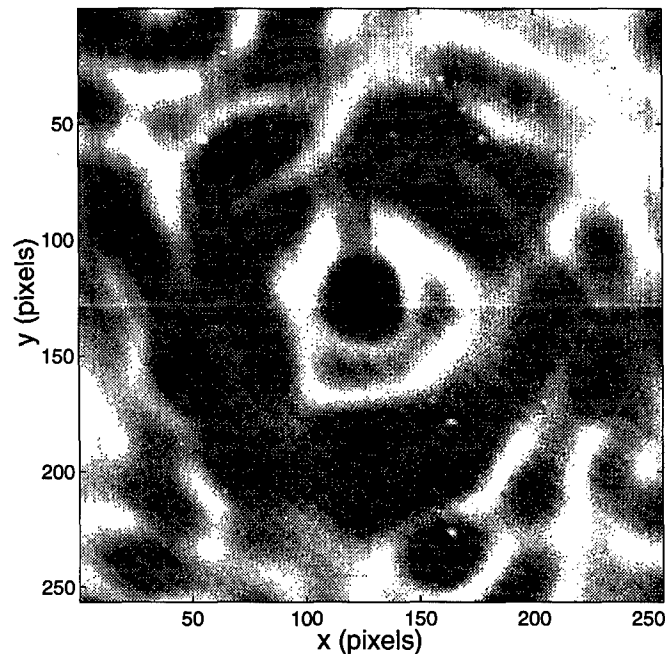off the MEMS in an undeflected and then biased position.

84

Figure 43. PSF of corrected aberration.

Using the reconstructed phase from Figure 33, we calculated the voltages required to deflect the mirrors about their bias position to match the aberrated wave front. Applying those voltages resulted in the PSF shown in Figure 43. Nothing too dramatic is noted from initial examination of the corrected PSF. Comparing to Figure 41, we can note some better definition of the off-center lobes: they are better connected and better defined as they encircle the central order. But it is difficult to directly compare the CCD images presented here, because they are normalized to different values.

A more direct comparison results from a plot of the radial average intensity for the PSF. Figure 44 shows the radial average intensity of the corrected reflection with the original uncorrected aberration of Figure 39 (no bias voltage). The improvement in the PSF is primarily concentrated in the increased central peak intensity, a rise seen to be about 43 percent. The relative lowering of the intensities in the off-center peaks is also noted. Examination of the aberrated PSF in Figure 39 shows that it has lost intensity in its first Airy ring: the region surrounding the central order is very low in intensity. But
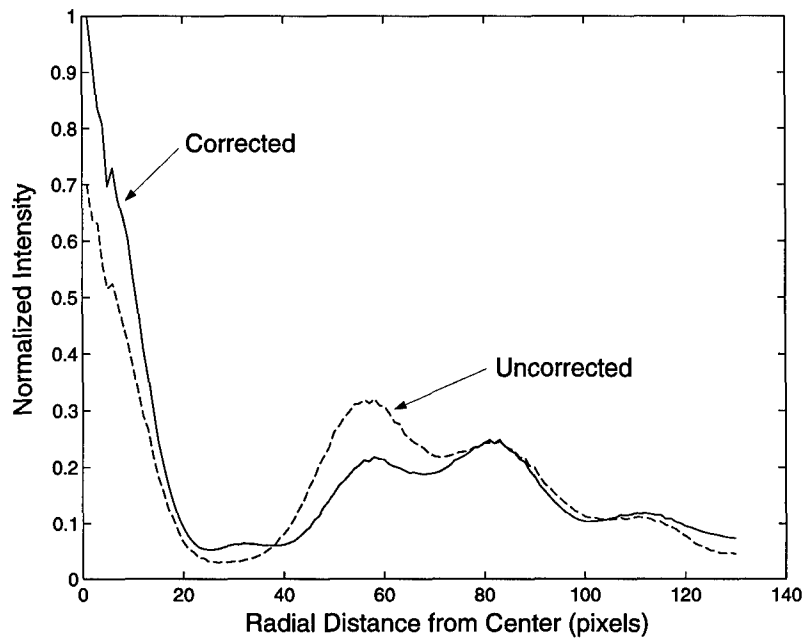
Figure 44.   Comparison of the radial average PSF intensity for the corrected and uncorrected aberration MEMS reflections.

in the corrected PSF, we note the reappearance of the ring, although it is not uniform. Figure 44 shows a hump in the solid line (corrected aberration) just after the initial peak falls to its minimum. Such a feature is noticeably absent from the dashed line. These results encourage us to conclude that we have demonstrated some degree of success in correcting the aberration.

The relative lowering of off-center peak intensities is consistent with an improvement in the reflected aberration, as shown by comparison with Figure 36. The plane mirror reflections showed that the aberration tended to significantly increase the relative intensity of the off-center lobes. This same effect is seen in Figure 40 for the case of the MEMS reflections. Furthermore, we notice a decrease of about a pixel in the full-width, half-maximum of the central peak between the corrected and uncorrected cases in Figure 44, as we expect. These results are not too dramatic, but they are consistent, and they show improvement in the degree of aberration.

If we compare our corrected, peak PSF value from Figure 44 to the unaberrated peak value in Figure 40, we see that we would have a corrected peak that is 0.14 times the unaberrated peak (a 43 percent improvement). Based on the modeling work performed by Roberts [28], we did not expect to achieve a complete correction of the wave front aberration. Taking an unaberrated MEMS reflection as producing an intensity of 1.0 (the same as for Figure 40), Roberts' model showed that we should expect the central order's peak value from the corrected aberration reflection to be about 0.15 of the unaberrated intensity. This is in excellent agreement with our demonstrated improvement.

However, it serves to show that these bare MEMS devices may not be well suited for general application in adaptive optics systems. One obvious limitation is that the active control surfaces are limited to 48 percent of the total MEMS area (see Table 3). Thus, there will be discontinuities in the mirror surface that we cannot control. Additionally, the flexure arms themselves are of significant size when compared to a HeNe wavelength, and they introduce additional changes in the reflected wave front as their position and angling is altered.

There exists a system design alternative that will overcome the limited active surface area available with MEMS devices. It involves the use of a lenslet array, positioned in front of a MEMS, so that the incoming light is spatially sampled and focused onto individual mirrors, thus eliminating the effects of mirror segmentation [17]. This recommendation is more fully explored in the following chapter.

V. Conclusions and Recommendations

The demonstration showed improvements in the PSF of a spherically aberrated plane wave by using a MEMS mirror array as a deformable mirror to correct the incident aberration. This was the first known demonstration of its kind. The changes in the PSF noted for the corrected aberration measurements were consistent with an improvement in the spherical aberration. The most dramatic features were a 43 percent rise in the peak intensity of the central diffraction order, and a reduction in the relative intensity of the off-center lobes. Additionally, the aberration tended to obliterate the first Airy-like ring of the unaberrated PSF, and the corrected images managed to restore portions of the feature.

However, the MEMS device used by this demonstration is clearly not ideal for performing aberration correction in real applications. Figure 37 shows that the MEMS reflections resulted in large number of diffraction orders in the PSF that only serve to take energy away from the central order. In low-light level applications, this is not a tolerable effect. New designs or implementations will have to be developed before MEMS micro-mirror arrays are to be implemented in real adaptive optics systems.

The discontinuous nature of segmented mirrors is a hindrance for their use in adaptive optics applications unless a large percentage of active surface can be achieved. For the particular devices used in this research, the relatively small amount of active control surfaces (48 percent) certainly hindered better results. Additionally, the curvature of each mirror tended to focus each portion of the field upon reflection. This effectively added more aberrations to the field that would not otherwise be present if planar mirrors were utilized. Finally, an accurate and complete characterization of the mirror response to voltage (i.e. determination of $\hat{k}$ for use in Equation 69) would certainly have helped establish an accurate bias position for each mirror about a 2π reflection point.

A more promising new design will manufacture a MEMS micro-mirror array for use with a lenslet array (the same type used for the Hartmann WFS) [17]. By positioning the MEMS device behind the lenslet array, an incident wave front will be spatially sampled and focused onto the individual mirror elements. The mirrors can then be adjusted to compensate for the phase perturbations of the incident field. Upon reflection, the field will

pass back through the lenslet array and recombine to form a continuous field once again. This technique effectively masks the discontinuous nature of the MEMS, and it should dramatically reduce the intensity of the higher diffraction orders in the PSF. A potential problem with the design proposal is that some light will be lost by portions of the reflected field that do not reflect exactly back through the lens they entered.

The primary advantage of MEMS devices as deformable mirrors is their use of electrostatic actuators. Electrostatic actuators are smaller and inherently faster than their piezo-electric counterparts, and MEMS construction techniques are cheaper. The use of the actuators in a segmented mirror configuration is a natural consequence of the standard MEMS construction techniques. But nothing fundamental limits their use to segmented deformable mirrors. Continuous membrane designs have been built by Texas Instruments [15], but they are not ideal for use in adaptive optics applications. Further research into continuous facesheet MEMS designs is definitely warranted.

As demonstrated by this research, the use of MEMS devices as deformable mirrors in adaptive optics systems holds promise. For all the difficulties encountered with the devices used, they performed in a manner consistent with an improvement in the PSF of the reflected field. New designs will certainly result in better performance, and it is hoped that this research will provide some impetus to proceed down a path that will lead to more dramatic results.

Bibliography

1. M. C. Roggemann, B. Welsh, *Imaging Through Turbulence*, New York: CRC Press, 1996.

2. F. Roddier, "The effects of atmospheric turbulence in optical astronomy," in *Progress in Optics* (E. Wolf, ed.), vol. XIX, New York: North-Holland, 1981.

3. J. W. Hardy, "Active optics: a new technology for the control of light," *Proc. IEEE*, vol. 66, pp. 651–697, 1978.

4. J. W. Hardy, "Adaptive optics – a progress review", in *Proc. SPIE on Active and Adaptive Optical Systems*, vol. 1542, pp. 2–17, 1991.

5. M. A. Ealey, J. F. Washeba, "Continuous facesheet low voltage deformable mirrors," *Opt. Eng.*, vol. 29, no. 10, pp. 1191–1198, 1990.

6. B. Hulburd, D. Sandler, "Segmented mirrors for atmospheric compensation," *Opt. Eng.*, vol. 29, no. 10, pp. 1186–1190, 1990.

7. T. A. Rhoadarmer, V. M. Bright, B. M. Welsh, S. C. Gustafson, and T. H. Lin, "Interferometric characterization of the flexure beam micromirror device," *Proc. SPIE*, vol. 2291, pp. 13–23, 1994.

8. J. H. Comtois, *Structures and techniques for implementing and packaging complex, large scale microelectromechanical systems using foundry fabrication processes*, AFIT Thesis, 1996.

9. M. A. Michalicek, *Design, fabrication, modeling, and testing of surface-micromachined micromirror devices*, AFIT Thesis, 1995.

10. D. R. Pape, L. J. Hornbeck, "Characteristics of the deformable mirror device for optical information processing," *Opt. Eng.*, vol. 22, no. 6, pp. 675–681, 1983.

11. W. R. Wu, R. O. Gale, L. J. Hornbeck, J. B. Sampsell, "Electro optical performance of an improved deformable mirror device," *Proc. SPIE*, vol. 825, pp. 24–31, 1987.

12. R. M. Boysel, J. M. Florence, W. R. Wu, "Deformable mirror light modulators for image processing," *Proc. SPIE*, vol. 1151, pp. 183–194, 1989.

13. T. H. Lin, "Implementation and characterization of a flexure-beam micromechanical spatial light modulator," *Opt. Eng.*, vol. 33, no. 11, pp. 3643–3648, 1994.

14. K. E. Peterson, "Micromechanical light modulator array fabricated on silicon," *Appl. Phys. Lett.*, vol. 31, no. 8, pp. 521–523, 1977.

15. L. J. Hornbeck, "128 x 128 Deformable Mirror Device," *IEEE Trans. on Elec. Dev.*, vol. ED-30, no. 5, pp. 539–545, 1983.

16. C. J. Christensen, *Micromirror array control of a phase-locked laser diode array*, AFIT Thesis, 1995.

17. S. C. Gustafson, G. R. Little, V. M. Bright, J. H. Comtois, E. W. Watson, "Micromirror arrays for coherent beam steering and phase control," to be published in *Proc. SPIE*, vol. 2881, no. 5, 1996.

18. E. A. Watson and A. R. Miller, "Analysis of beam steering using phased micromirror arrays," *Proc. SPIE*, vol. 2687, no. 8, 1996.

19. H. W. Babcock, "The possibility of compensating astronomical seeing," *Publ. Astron. Soc. Pac.*, vol. 65, pp. 229–236, 1953.

20. B. A. Horwitz, "Multiplex techniques for real-time shearing interferometry," *Opt. Eng.*, vol. 29, pp. 1223–1232, 1990.

21. J. W. Hardy, A. J. MacGovern, "Shearing interferometry: a flexible technique for wavefront measurement," *SPIE Proceedings on Interferometric Metrology*, vol. 816, pp. 180–195, 1987.

22. G. Rousset, "Wavefront sensing", in *Adaptive Optics for Astronomy* (D. Alloin and J.-M. Mariotti, eds.), vol. C423 of *NATO Advanced Study Institute Series*, pp. 115–137, Kluwer Academic Publishers, 1994.

23. T. J. Kane, B. M. Welsh, C. S. Gardner, and L. A. Thompson, "Wave front detector optimization for laser guided adaptive telescopes," in *SPIE Proceedings on Active Telescope Systems*, vol. 1114, pp. 160–171, 1989.

24. G. Cao and X. Yu, "Accuracy analysis of a hartmann-shack wavefront sensor operated with a faint source," *Opt. Eng.*, vol. 33, pp. 2331–2335, 1994.

25. M. C. Roggemann, P. J. Gardner, B. M. Welsh, R. D. W. Bowersox, D. W. Jewell, "Gas flow visualization by means of sheared beam interferometry: sensitivity, maximum measurable gradient of the density fluctuation, and integrated density estimation," accepted for publication by *Measurement*.

26. T. H. Lin, "Flexure-beam micromirror devices and potential expansion for smart machining," *Proc. SPIE*, vol. 2722, pp. 20–29, 1996.

27. S. C. Gustafson, T. A. Tuthill, and E. A. Watson, "Micromirror arrays for active optical aberration control," *Proc. SPIE*, vol. 2687, no. 02, 1996.

28. P. Roberts, "Modeling and simulation of optical characteristics of microelectromechanical mirror arrays", AFIT Thesis, 1996.

29. J. D. Gaskill, *Linear Systems, Fourier Transforms, and Optics*, New York: John Wiley & sons, 1978.

30. J. W. Goodman, *Introduction to Fourier Optics*, 2nd ed., New York: McGraw-Hill, 1996.

31. E. P. Wallner, "Optimal wave front correction using slope measurements," *J. Opt. Soc. Am.*, vol. 73, pp. 1771-17776, 1983.

32. M. A. Michalicek, V. M. Bright, and J. H. Comtois, "Design, fabrication, modeling, and testing of a surface-micromachined micromirror device," *Proc. of the ASME Dynamic Systems and Control Division*, vol. 57, no. 2, pp. 981–988, 1995.

33. "Zygo Maxim-3D, Operation and Maintenance Manual, OMP-0256," Zygo Corporation: Middlefield, CN, November, 1988.

Vita

Shaun Roger Hick ~~████████████████████████~~ to E. Roger and Susan Hick. By the time Shaun was ready to start school, the Hicks had settled in Bay Village, Ohio, where Shaun completed his primary education. He graduated from Bay High School in June, 1988, and was accepted for undergraduate study at the University of Michigan, in Ann Arbor. Having received an Air Force ROTC scholarship, Shaun joined Detachment 390, eventually becoming the Cadet Group Commander during the first semester of his senior year. Shaun graduated from UM in May, 1992 with a Bachelor of Science degree in Physics. A Distinguished Graduate from ROTC, he was commissioned a second lieutenant in the Air Force upon graduation.

Shaun's first assignment was at the National Air Intelligence Center, Wright-Patterson AFB, OH, beginning in November, 1992. Shaun worked in the acquisition support branch, providing technical intelligence support to various acquisition programs, including the Reconnaissance System Program Office. While at NAIC, Shaun married the former René Thompson of Taylor, Michigan on August 14, 1993.

Shaun was then selected to attend AFIT, where he started the Applied Physics program in May, 1995. The promotion to his current rank of Captain occurred in August, 1996, and he graduated from AFIT the following December with a Master of Science degree in Applied Physics. His assignment after AFIT is to Wright Laboratories, Armament Directorate at Eglin AFB, FL where he anticipates working in the laser radar branch.